Intestinal Responses to Benzalkonium Chloride Exposure: Insights from Primary Human Enteroid Monolayers

Scott Alan Katz

A thesis submitted in partial fulfillment of the requirements for the degree of:

Master of Science

University of Washington

2026

Committee:

Libin Xu

Edward J. Kelly

Program Authorized to Offer Degree:

Environmental and Occupational Health Sciences

University of Washington

Abstract

Intestinal Responses to Benzalkonium Chloride Exposure: Insights from Primary Human Enteroid Monolayers

Scott Katz

Co-Chairs of the Supervisory Committee:

Libin Xu

Department of Medicinal Chemistry

Edward J. Kelly

Department of Pharmaceutics

Benzalkonium chlorides (BACs) are cationic surfactants present in hundreds of products, with human exposure rising in recent years. Despite widespread use and unintended ingestion, the direct effects of BACs on the human intestinal epithelium remain understudied. Primary human enteroid monolayers from three independent donors were used to assess transcriptional and barrier responses to acute and chronic BAC exposure. RNA-sequencing revealed that acute 16-hour exposure to a commercially relevant $C_{12}/C_{14}/C_{16}$ BAC mixture elicited robust transcriptional responses in two of three donors, including coordinated upregulation of cell cycle progression, cholesterol biosynthesis, and xenobiotic metabolism pathways. Substantial inter-donor variability in response magnitude underscores the value of primary human models for capturing individual differences in susceptibility. In contrast, chronic BAC cocktail exposure

over 16 days showed minimal transcriptional adaptation and barrier integrity changes, consistent with epithelial adaptation rather than cumulative toxicity. These findings position primary enteroid monolayers as a valuable platform for intestinal toxicology and highlight the need for further characterization of BAC exposure at the site of first oral contact.

Acknowledgements

The author wishes to thank the members of the Xu Lab and Kelly Lab for their support throughout this project. Special thanks are owed to Libin Xu, PhD, and Edward Kelly, PhD, for their mentorship and guidance as thesis advisors and committee members. The author appreciates the support from Kai Wang, MS, and Eimear O'Mahony on assistance with cell culture. The author also thanks Vanessa Lopez, PhD, Marie Brzoska, PhD, and Ryan Seguin, PhD, for contributions to mass spectrometry analysis, and the UW EDGE Center, particularly Theo Bammler and James MacDonald, for bioinformatics support. Confocal imaging was performed with the assistance of Dale Haley at the UW Institute for Stem Cells and Regenerative Medicine (ISCRM) and Garvey Imaging Institute. Intestinal organoid lines were generously provided by Mark Donowitz, MD (Johns Hopkins University) and Jason Smith, MD (University of Washington). This work was supported by the National Institute of Environmental Health Sciences (R01ES035021) and a pilot grant award from the University of Washington Interdisciplinary Center for Exposure, Diseases, Genomics, and Environment (EDGE), Department of Environmental and Occupational Health Sciences, University of Washington School of Public Health (P30ES007033).

Table of Contents

1. Introduction

1.1 Quaternary Ammonium Compounds & Benzalkonium Chlorides

Quaternary ammonium compounds (QACs) are a broad class of cationic surfactants defined by a central nitrogen atom bearing four substituents, yielding a permanently positively charged structure that has potent disinfectant properties (Merchel Piovesan Pereira & Tagkopoulos, 2019). Encompassing numerous chemical subclasses, QACs are among the most widely deployed antimicrobials in modern use, found in household disinfectants, industrial sanitizers, personal care products, pharmaceutical formulations, and even food processing facilities (Arnold et al., 2023). In recent years, QACs were formally characterized as a chemical

class of emerging concern by the California Environmental Protection Agency, owing to their widespread utilization, potential for bioaccumulation, and growing evidence linking systemic exposure to adverse health outcomes (California EPA, 2024). Critically, QACs are not currently monitored by the National Health and Nutrition Examination Survey (NHANES), leaving substantial gaps in our understanding of population-level exposure and associated epidemiological risk (Arnold et al., 2023; CDC, 2025). Despite widespread commercial use, the Food and Drug Administration (FDA) has not made a formal determination that QACs are Generally Recognized As Safe and Effective (GRAS/GRAE), repeatedly deferring rulemaking and calling for additional safety studies (FDA, 2019).

Among QAC subclasses, benzalkonium chlorides (BACs) have emerged as compounds of toxicological interest. BACs are characterized by a benzyl group, two methyl groups, and an alkyl chain ranging from C_8 to C_{18} in length (Figure 2.1). Notably, a commonly used $C_{12\text{-}16}$ BAC mixture (CAS#: 68424-85-1) is present in hundreds of consumer and occupational products: household disinfectants, surface cleaners, and food-contact surface sanitizers, reflecting widespread potential for human exposure (EPA, 2026). The COVID-19 pandemic dramatically accelerated BAC usage, as heightened public concern over surface transmission drove exponential increases in disinfectant consumption globally (Li et al., 2020). The biological consequences of this exposure surge were measurable: median blood-serum BAC levels rose by 174% during the pandemic compared to pre-pandemic baselines, a striking indication that increased use translated directly to elevated systemic concentrations (Zheng et al., 2021). Specifically, BACs have been detected in human blood-serum in low nanomolar concentrations, and in human feces from nanomolar to low micromolar levels (Li & Kannan, 2024; Zheng et al., 2021).

Human exposure to BACs occurs through multiple routes, with oral ingestion representing a particularly relevant but underappreciated pathway. Hand-to-mouth transfer following contact with disinfected surfaces, consumption of food prepared on BAC-sanitized food-contact surfaces, and direct ingestion of BAC residues contribute to oral exposure. Furthermore, children have age-specific behaviors that may make them more susceptible to oral exposure to BACs compared to adults (Zheng et al., 2021). BACs have been detected in consumer products at active ingredient concentrations typically ranging from 0.1% to 0.5%, while environmental monitoring has identified BAC in surface water, wastewater effluent, and household dust at concentrations in the low μg/L and μg/g range, respectively (EPA, 2026; Merchel Piovesan Pereira & Tagkopoulos, 2019). Following oral ingestion, the small intestine represents the primary site of first-contact exposure, where luminal BAC concentrations may substantially exceed those in systemic circulation (Lee et al., 2014). Thus, characterizing BAC disposition in the small intestine is critical for understanding the potential for direct intestinal toxicity.

The *in vitro* metabolic fate of BACs has begun to be characterized, though primarily in hepatic model systems. BACs undergo CYP-mediated oxidative metabolism along the alkyl chain in human liver microsomes, with metabolic stability increasing with chain length and hydroxylated metabolites displaying markedly reduced capacity to inhibit cholesterol biosynthesis relative to the parent compound, suggesting a detoxifying role for CYP-mediated clearance (Seguin et al., 2019). Furthermore, longer chain BACs have demonstrated inhibition of renal organic cation transporters hOCT1-3 and hMATE1/2K, yet short-chain congeners (C_8 and C_{10}) are substrates of these same transporters (Vieira et al., 2024).

The toxicological profile of BACs has been investigated across multiple organ systems and exposure contexts, revealing a breadth of adverse effects. Historical case reports have shown that acute high-dose ingestion of BAC-containing formulations has been associated with fatal outcomes (Hitosugi et al., 1998; Wilson & Burr, 1975). At lower, more environmentally relevant concentrations, BAC exposure has been linked to sensitization reactions affecting the skin, respiratory tract, and immune system, as well as occupational asthma in healthcare and cleaning workers (AOEC, n.d.; Arnold et al., 2023; Wentworth et al., 2016). *In vivo* studies have demonstrated reproductive and developmental toxicity, including reduced fertility and neural tube defects following ambient QAC exposure (Hrubec et al., 2017; Melin et al., 2014). At a systemic and biochemical level, BAC exposure has been associated with nephrotoxicity (Brzoska et al., 2026), inflammation (Hrubec et al., 2021), disruption of gut microbial communities (Lopez et al., 2024), and alterations in cholesterol, lipid, and bile acid homeostasis (Herron et al., 2019).

There is limited research regarding the direct impact of BACs on the intestine. *In vivo* BAC exposure has been associated with structural intestinal injury including villus impairment, goblet cell depletion, and upregulation of the tight junction protein claudin-2, as well as increased tumor cell proliferation and suppressed apoptosis in colorectal tumor tissue, collectively suggesting BAC bioactivity extends to disruption of intestinal epithelial homeostasis (Feng et al., 2025; Sanidad et al., 2018). Yet, each of these studies relied on supraphysiological doses or models not directly translatable to humans. Consequently, whether comparable responses occur in the human intestinal epithelium at relevant exposure concentrations remains understudied.

1.2 Small Intestine

The small intestine is a critical site of environmental toxicant disposition and represents the primary barrier between ingested compounds and systemic circulation. For orally consumed chemicals, the intestinal epithelium constitutes one of the first points of contact prior to absorption, where luminal concentrations may far exceed those ultimately detected in blood or peripheral tissues (Gelberg, 2018). Structurally, the small intestine is divided into three proximal to distal segments: the duodenum, jejunum, and ileum, each with distinct functional properties and regional variation in transporter and enzyme expression (Campbell et al., 2019). Beyond its well-established roles in nutrient absorption and digestion, the small intestine maintains epithelial barrier integrity, contributes to mucosal immune defense, and participates in the first-pass extraction of drugs and xenobiotics through expression of drug metabolizing enzymes and transporters (DMET) (Gelberg, 2018).

The intestinal epithelial cell population is highly dynamic, undergoing complete renewal approximately every three to five days and being organized into crypt-villus units (Flier & Clevers, 2009). LGR5+ intestinal stem cells serve as the progenitor population of the small intestine, residing and proliferating within the crypts before migrating up the crypt-villus axis as they differentiate into the specialized cell types lining the villus surface (Clevers, 2013; Flier & Clevers, 2009). These include columnar enterocytes, which perform the bulk of nutrient absorption, as well as secretory lineages including goblet cells, enteroendocrine cells, and Paneth cells (Clevers, 2013). Fully differentiated cells are ultimately shed into the intestinal lumen, completing the cycle of continuous epithelial renewal. The canonical Wnt/β-catenin pathway serves as the primary driver of LGR5+ stem cell renewal in the crypt, where its activation leads to transcription of proliferative target genes including *LGR5*, *CCND1*, and *MYC* (Vanuytsel et al., 2013). *MYC* functions as a central downstream effector of canonical Wnt signaling, driving

cell cycle progression and crypt progenitor expansion, while its deletion has been shown to mitigate canonical Wnt-driven hyperproliferation (Sansom et al., 2007). Conversely, BMP/TGF-β signaling acts as a homeostatic brake on stem cell self-renewal with subsequent suppression of PI3K-Akt activity (Vanuytsel et al., 2013). Maintaining this balance between stem cell proliferation and terminal differentiation is therefore essential for preserving barrier integrity and sustaining the absorptive and secretory functions of the small intestine. Disruption of these pathways has direct toxicodynamic implications for how environmental contaminants perturb intestinal homeostasis.

The intestinal epithelial barrier is reinforced by tight junction complexes that are critical regulators of paracellular permeability and barrier integrity. These complexes consist of transmembrane proteins, including occludin and claudins, anchored to the cytoskeleton via cytoplasmic scaffolding proteins such as ZO-1 and ZO-3 (Barbara et al., 2021). Beyond their structural role as a physical barrier, tight junctions facilitate rapid cell-cell communication and contribute to the maintenance of epithelial polarity along the gastrointestinal tract (Barbara et al., 2021). Disruption of tight junction integrity is a well-established mechanism of enterotoxicity, with downstream consequences including increased permeability to exogenous pathogens and ingested toxicants, dysbiosis of the gut microbiome, and altered bioavailability of drugs. Despite this vulnerability, the direct effects of QACs such as BACs on the intestinal epithelium remain poorly characterized, in part due to the absence of physiologically relevant human model systems capable of capturing both the cellular complexity and barrier properties of the native tissue.

1.3 Primary Human Enteroid Monolayer Model

Addressing this gap requires an experimental model that recapitulates the multicellular composition, polarized architecture, and barrier function of the human intestinal epithelium. The

development of intestinal organoid culture systems has fundamentally transformed the study of intestinal epithelial biology. It was first demonstrated that murine Lgr5+ intestinal stem cells isolated from crypts could self-organize into three-dimensional (3D) organoids, recapitulating crypt-villus architecture and cellular diversity *in vitro* (Sato et al., 2009). This technology has extended into humans, enabling generation of patient-derived intestinal organoids, referred to as enteroids, from biopsies (Sato et al., 2011). While 3D enteroid cultures are promising for cell and molecular biology studies, their enclosed architecture presents a significant limitation for their pharmacokinetic and toxicological applications. In three-dimensional cultures, the apical surface of the epithelium faces the inside of each organoid, rendering it largely inaccessible to dosed compounds without manipulation or microinjection (Sato et al., 2009). While certain techniques have been shown to evert this architecture (Co et al., 2019), many challenges remain for microcellular scaling. This is a critical constraint when studying luminal xenobiotics such as BACs, which encounter the apical surface of columnar enterocytes following oral ingestion.

To overcome these limitations, protocols have been developed to enzymatically or mechanically dissociate the three-dimensional enteroids and re-plate the resulting single-cell suspension as two-dimensional monolayers atop collagen-coated Transwell inserts (Arian et al., 2022). This configuration inverts the orientation of the epithelium, forming properly polarized monolayers by exposing the apical membrane to the media and the basal surface attached to a permeable membrane which enables direct dosing of xenobiotics without the need for microinjection (Arian et al., 2022; O'Mahony et al., 2025). The resulting monolayers retain the multicellular composition characteristic of the intestinal epithelium *in vivo*: columnar enterocytes, goblet cells, enteroendocrine cells, and Paneth cells (Arian et al., 2025). The functional integrity and utility of human enteroid monolayers have also been demonstrated.

Barrier formation, as measured by transepithelial electrical resistance (TEER), stabilizes after differentiation within the Transwell and has been shown to persist for at least 42 days in culture (Arian et al., 2025). Barrier integrity is also verified with low paracellular permeability by fluorescent probes such as lucifer yellow (Arian et al., 2025). Beyond structural characterization, the extended culture viability of enteroid monolayers facilitates long-term exposures and improves the basis for *in vitro*-to-*in vivo* extrapolation (IVIVE), while the Transwell format enables direct assessment of changes in barrier integrity in response to drugs or toxicants. In addition to robust barrier integrity, enteroid monolayers maintain expression, inducibility, and activity of drug-metabolizing enzymes, including CYP3A, and the model has since been applied to characterize the effects of inflammatory stimuli on intestinal drug transporter expression, representing a significant advance over historically used *in vitro* intestinal models (Arian et al., 2025; Wang et al., 2026). Together, these elements position the human enteroid monolayer as a functionally stable, physiologically relevant *in vitro* platform of the intestinal epithelium.

Relative to traditionally used *in vitro* intestinal models such as Caco-2 cells, human enteroid monolayers offer critical advantages for toxicological applications. Caco-2 cells are derived from human colorectal adenocarcinoma and represent a homogeneous, transformed cell population that incompletely recapitulates the cellular diversity, transporter expression, and metabolic capacity of the native small intestine (Jeong et al., 2025; Sun et al., 2008). By contrast, primary enteroid monolayers are non-cancerous cultures derived directly from human biopsies, preserving the complement of enteric cell types and the donor-specific biological variability (O'Mahony et al., 2025). This is consequential for studying environmental toxicants such as BACs, where inter-individual variation in susceptibility and metabolism represents a key knowledge gap. Furthermore, human enteroid monolayers are a new approach methodology,

aligning with the principles of the 3Rs framework: replacement, reduction, and refinement of animal testing. In the context of the present study, the primary human enteroid monolayer represents an ideal model system for characterizing the intestinal response to oral BAC exposure. This system enables apical and basolateral dosing at physiologically relevant concentrations in a model that recapitulates the structural and functional properties of the human small intestine.

The present study sought to characterize the transcriptional and barrier responses of primary human intestinal epithelium to benzalkonium chloride exposure using a duodenal enteroid monolayer model. Specifically, we aimed to: (1) establish and validate primary human enteroid monolayers as a functionally intact platform for toxicological dosing; (2) define the acute transcriptional response to exposure with a commercial BAC mixture across a range of physiologically relevant concentrations; and (3) determine whether chronic, repeated BAC exposure produces cumulative transcriptional disruption or barrier dysfunction. By integrating RNA sequencing with additional measures of barrier integrity across multiple human donors, this study provides insight into how the intestinal epithelium responds and adapts to exposure to a widely used class of disinfectants at the site of primary contact.

2. Materials and Methods

2.1 Chemicals and Reagents

IntestiCult Organoid Growth Medium (Human) and IntestiCult Organoid Differentiation Medium (Human) were purchased from STEMCELL Technologies (Vancouver, BC). Individual benzalkonium chloride congeners were purchased from Sigma-Aldrich (St. Louis, MO): C_{12}-BAC (cat. no. 13380), C_{14}-BAC (cat. no. M401), and C_{16}-BAC (cat. no. B4136). Advanced Dulbecco's Modified Eagle Medium/F-12 (Advanced DMEM/F12), TrypLE Express, Dulbecco's

phosphate-buffered saline with calcium and magnesium (DPBS++), Hanks' Balanced Salt Solution with calcium and magnesium (HBSS++), Hoechst 33342, ProLong Gold Antifade Reagent, PureLink DNase, and dimethyl sulfoxide (DMSO) were purchased from Thermo Fisher Scientific (Waltham, MA). Penicillin-streptomycin (10,000 U/mL) was purchased from Life Technologies (Carlsbad, CA). Matrigel Growth Factor Reduced Basement Membrane Matrix (phenol red-free, lactate dehydrogenase [LDH] elevating virus-free), collagen IV, Cell Recovery Solution (CRS), and 24-well Transwell permeable inserts were purchased from Corning (Corning, NY). Y-27632 (dihydrochloride) and lucifer yellow (LY) dipotassium salt were purchased from MedChem Express (Monmouth Junction, NJ). The RNeasy Mini Kit was purchased from Qiagen (Germantown, MD). Normal goat serum was purchased from Vector Laboratories (Newark, CA). Triton X-100 was purchased from Research Products International (Mt. Prospect, IL). Tween-20 was purchased from Fisher Scientific (Hampton, NH). Primary and secondary antibodies are listed in Supplementary Table 1.

2.2 Three-Dimensional Enteroid Culture

Duodenal crypts from 3 independent donors (Table 2.1) isolated via endoscopy for clinically indicated conditions, where the upper gastrointestinal tract was endoscopically normal, were provided by Dr. Mark Donowitz, MD (Johns Hopkins University, Baltimore, MD) and Dr. Jason Smith (University of Washington, Seattle, WA). The original biopsy samples were collected in accordance with the institutional review board of John’s Hopkins University (protocol numbers IRB-NA_00038329 and IRB-00044373). Undifferentiated organoids derived from these crypts were thawed and cultured in Matrigel domes in 24-well cell culture plates in the presence of 0.5 mL Intesticult Organoid Growth Medium (Human) supplemented with 1% (v/v) penicillin-streptomycin (herein referred to as OGM). All organoids were grown in Matrigel

normalized to a concentration of 4.6 mg/mL and the media was changed every 2-3 days until > 90% confluency (Supplementary Figure 1A). Organoids were passaged every 5-10 days, where Matrigel domes were broken by adding 0.5 mL of Cell Recovery Solution (CRS), followed by shaking for 30 minutes at 4 ºC on an orbital shaker. The cell slurry was mechanically broken up by pipetting up and down until approximately 80% of the organoids were dissociated. The cells were collected, and each well was washed with 0.5 mL Advanced DMEM/F12. The dissociated cell suspension was centrifuged at 1200 x g for 10 minutes, the supernatant was discarded, and the resulting pellet was resuspended in Matrigel. Cells were plated in 50 µL Matrigel dome plugs in 24-well culture plates and incubated at 37 ºC for 15-20 minutes to allow Matrigel® polymerization. The domes were subsequently overlaid with 0.5 mL of OGM, pre-warmed to 37ºC, supplemented with 10 µM of Y-27632 (dihydrochloride), a Rho-associated protein kinase inhibitor, to begin a new passage cycle. Penicillin-streptomycin was added to OGM for thawing, passaging, and media changes, whereas Y-27632 (dihydrochloride) was supplemented in OGM only during thawing and passaging.

Table 2.1. Human Intestinal Organoid Donor Characteristics.

Donor Identification Name	Age	Sex	Passage(s)	Purveyor
HDO03	68	Male	23	J. Smith
HDO07	70	Female	13-19	J. Smith
HDO11	27	Female	58	M. Donowitz

2.3 Seeding into Two-Dimensional Enteroid Monolayers

Prior to seeding, Transwell inserts were coated with 100 µL Collagen IV diluted to 0.034 mg/mL in DPBS++ and incubated at 37 ºC for a minimum of 8 hours to allow coating adsorption. For monolayer generation, 3D organoid domes were first dissociated by adding 0.5

mL of Cell Recovery Solution, followed by gentle shaking at 4º C for 30 minutes with an orbital shaker. The cell suspension was collected, and each well was washed with 0.5 mL Advanced DMEM/F12, then centrifuged at 1200 x g for 10 minutes and the supernatant discarded. The pellet was then resuspended in 100 µL of TrypLE Express per well and incubated at 37 ºC for 5 minutes. Cell clumps were further dissociated by repeated pipetting, after which a 10-fold volume of cold DPBS++ was added to quench enzymatic activity. The single-cell suspension was then centrifuged at 1200 x g for 10 minutes, the supernatant was discarded, and the pellet was resuspended in IntestiCult Organoid Differentiation Medium supplemented with 1% v/v penicillin-streptomycin and 10 µM Y-27632 dihydrochloride (herein referred to as ODM). Prior to seeding the single-cell suspension as monolayers, the remaining DPBS++ was removed from the apical compartment of the Transwell and 0.5 mL of ODM was added basally. Then, the cells were seeded at a 1:1 Matrigel dome-to-insert ratio atop each collagen-coated Transwell by applying 100 µL of cell suspension in ODM to the apical compartment.

2.4 Monolayer Maintenance and Differentiation

Following seeding, media in both the apical and basolateral compartments was replaced every two days with fresh ODM. For acute exposures, monolayers were cultured for 14 days to allow for confluence and differentiation, with experiments performed on Day 14 of differentiation (Supplementary Figure 1B).

For chronic exposures, monolayers were cultured under the same conditions through Day 8 of differentiation, at which point BAC cocktail dosing was initiated. From Day 8 onwards, media changes were performed every two days with ODM supplemented with BAC cocktail at 50 nM, 500 nM, or 3 µM, or DMSO as a vehicle control. Cells were collected for downstream assays at Day 16 following the first dosing window and at Day 24 following the second dosing

window. A graphical abstract of experimental overview and culture conditions is shown in Figure 3.1.

2.5 Transepithelial Electrical Resistance

Transepithelial electrical resistance (TEER) was measured every two days prior to media changes throughout the 14-day differentiation period using an EVOM2 Epithelial Voltohmmeter (World Precision Instruments, Sarasota, FL). Prior to each measurement session, the probe was submerged in 70% ethanol diluted with ultrapure water for sterilization, followed by equilibration in Advanced DMEM/F12. A blank collagen-IV Transwell insert containing no cells was measured as a reference. Raw resistance values (Ω) were corrected by subtracting blank insert resistance and normalized to the Transwell membrane surface area (0.33 cm^2) to yield reported TEER values expressed in Ω•cm^2.

2.6 Lucifer Yellow Permeability

Paracellular permeability was assessed using lucifer yellow (LY) concurrently with BAC transport experiments on Day 14 of differentiation. Monolayers were washed three times with HBSS++ following aspiration of ODM, then dosed either apically with 10 µM LY in 200 µL HBSS++ (apical-to-basolateral) or basally with 10 µM LY in 500 µL HBSS++ (basolateral-to-apical). All samples were protected from light throughout the assay using aluminum foil. Following a 60-minute incubation at 37 °C, fluid was collected from both compartments into microcentrifuge tubes. Samples were transferred to a 96-well plate for fluorescence measurement; donor compartment samples were diluted 1:1 with HBSS++ while receiving compartment samples were transferred undiluted, for a final volume of 100 µL per well. LY fluorescence was measured using a fluorescence plate reader at excitation and emission

wavelengths of 428 nm and 536 nm, respectively. Paracellular permeability was expressed as percent diffusion, calculated relative to the apical donor concentration against a standard curve.

2.7 Immunocytochemistry

To evaluate morphology and cell polarity of differentiated enteroid monolayers, immunocytochemistry (ICC) was performed targeting zonula occludens-3 (ZO-3), occludin, multidrug resistance-associated protein 3 (MRP3), and Ki-67. Following completion of TEER measurements and lucifer yellow permeability assays, monolayers were washed three times with DPBS++ on both the apical and basolateral sides, then fixed with 200 µL 4% paraformaldehyde in DPBS++ for 15 minutes at room temperature. The monolayers were washed three additional times with cold DPBS++ and stored at 4 ºC for no longer than five days.

Monolayers stained for Ki-67 were permeabilized with 0.1% Triton X-100 in DPBS++ for 5 minutes at room temperature prior to blocking. No permeabilization step was used for the membrane proteins ZO-3, occludin, and MRP3. All monolayers were blocked with 1% normal goat serum and 0.05% Tween-20 in DPBS++ for 60 minutes at 4 ºC. The following primary antibodies were diluted 1:100 in blocking solution and incubated overnight at 4 ºC: rabbit anti-ZO-3 (ab181991, Abcam), mouse anti-occludin (ab242202, Abcam), rabbit anti-MRP3 (ab204322, Abcam), and rabbit anti-Ki-67 (ab92742, Abcam). The following day, monolayers were washed three times with 0.05% Tween-20 in DPBS++, with two washes performed under gentle agitation. The following secondary antibodies were diluted 1:1000 in blocking solution, centrifuged at 12,000 x g for 3 minutes to remove aggregates, and applied overnight at 4 ºC protected from light: goat anti-rabbit IgG Alexa Fluor 594 (A-11037, Invitrogen), goat anti-rabbit IgG Alexa Fluor 488 (A-11008, Invitrogen), and goat anti-mouse IgG Alexa Fluor 488 (A-

21141, Invitrogen). Monolayers were washed five times with gentle shaking, protected from light. Nuclei were counterstained with 0.5 µg/mL Hoechst 33342 (H3570, Invitrogen) in DPBS++ for 15 minutes at room temperature, followed by three additional washes with gentle shaking, protected from light. Transwell membranes were excised and mounted basolateral side down onto glass slides using ProLong Gold Antifade Reagent, and coverslips were sealed. Images were acquired the same day using a Nikon A1R laser-scanning confocal microscope at the University of Washington Institute for Stem Cell and Regenerative Medicine (ISCRM). Primary and secondary antibodies utilized are also listed in Supplementary Table 1.

2.8 Preparation of Benzalkonium Chloride Cocktail

Individual BAC congeners (C_{12}-, C_{14}-, and C_{16}-BAC) were each dissolved in DMSO to prepare distinct 50 mM stock solutions, which were stored at room temperature protected from light. Working solutions were prepared by combining three stocks at a fixed molar ratio of 40:50:10 (C_{12}:C_{14}:C_{16}; Figure 2.1), consistent with BAC congener distributions reported in commercial formulations (EPA, 2026), then diluted 1000-fold into ODM or HBSS++ prewarmed to 37 ºC, immediately prior to use. Final BAC cocktail concentrations tested in this study were 50 nM, 500 nM, and 3 µM, with a maximum DMSO concentration of less than 0.1%.

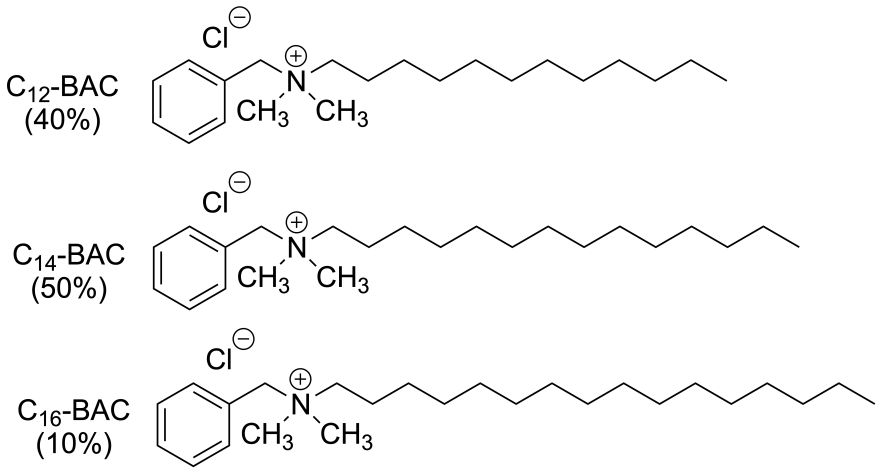

Figure 2.1. Chemical structures and molar composition of the BAC cocktail used in this study. C_{12}-, C_{14}-, and C_{16}-BAC congeners are shown with their respective molar proportions (40:50:10) within the prepared mixture.

2.9 RNA-sequencing

For 16-hour incubations, enteroid monolayers were exposed apically to the BAC cocktail at 50 nM, 500 nM, or 3 μM in pre-warmed ODM (37ºC, 100 μL per Transwell) on Day 14 of differentiation. For chronic exposures, enteroid monolayers were exposed apically to the same concentrations every other day, beginning at Day 8 of differentiation. Vehicle controls received an equivalent volume of DMSO-matched ODM. Following the exposure window, monolayers were lysed in 300 μL of RLT buffer and RNA was extracted using the Qiagen RNeasy Mini Kit according to the manufacturer's protocol. DNase treatment was performed using a PureLink DNase Kit to remove residual genomic DNA. RNA was eluted in 32 μL RNase-free water and quantified by NanoDrop spectrophotometry prior to submission. RNA integrity and concentration were subsequently confirmed by Novogene (Sacramento, CA) prior to library preparation. Libraries were prepared using poly-A enrichment and sequenced by Novogene on an Illumina platform in paired-end mode with 150 bp reads. Raw FASTQ files were assessed for quality using FastQC and MultiQC. Reads were aligned to the NCBI RefSeq GRCh38 human transcriptome and summarized to the gene level using the tximport package in R. Differential expression analysis was performed using limma-voom by the University of Washington EDGE center. For acute exposures, a significance threshold of FDR < 0.05 was applied. For chronic exposures, a relaxed threshold of FDR < 0.10 was applied given the limited number of DEGs detected. All conditions were prepared with four technical replicates.

3. Results

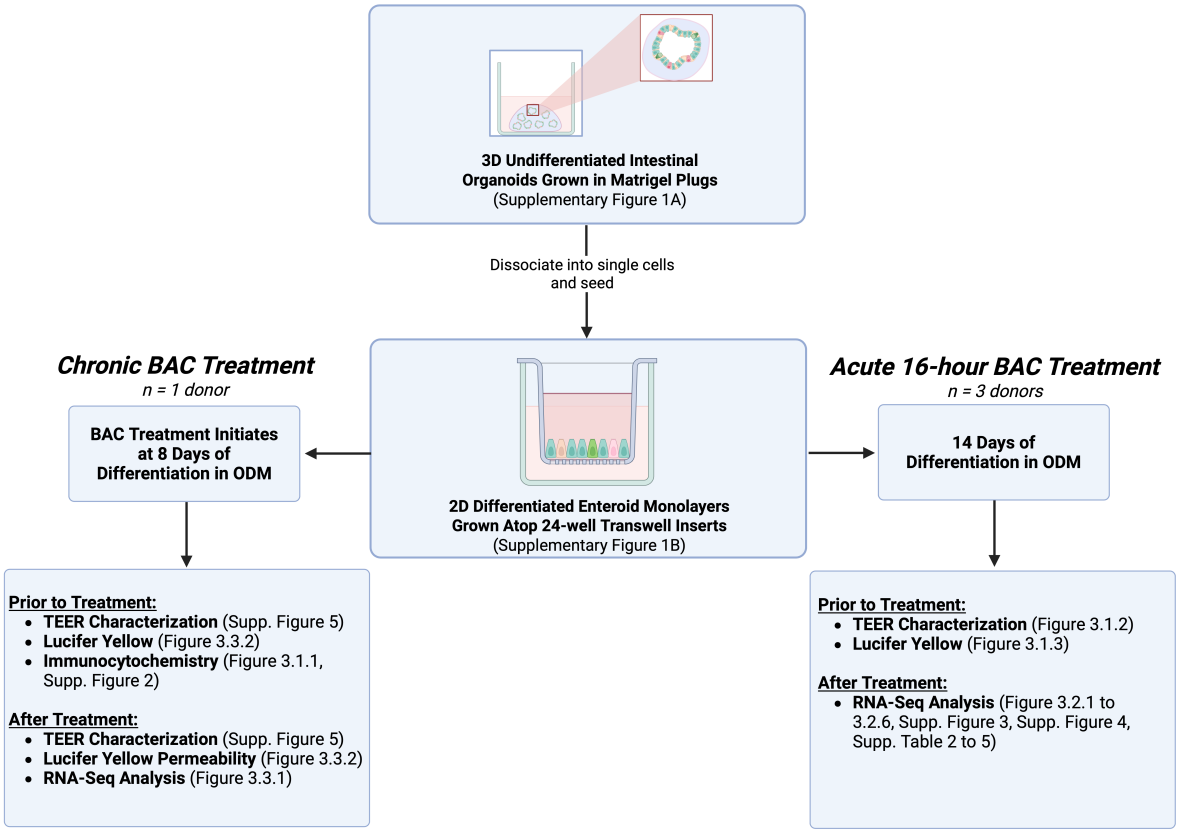

Figure 3.1. Experimental overview of chronic and acute 16-hour BAC treatment in primary human enteroid monolayers. Organoids were dissociated and seeded onto Transwell inserts for differentiation in ODM. Chronic (n = 1 donor) and acute 16-hour (n = 3 donors) BAC treatment arms were assessed for barrier integrity and transcriptional changes.

3.1 Enteroid Monolayer Model Characterization

Prior to evaluating the intestinal response to BAC exposure, enteroid monolayers were characterized to confirm structural organization and barrier integrity. Caco-2, an immortalized colorectal adenocarcinoma line, lacks the multilineage cellular diversity of primary intestinal epithelium and forms barriers with supraphysiological resistance, limiting its physiological relevance (Sun et al., 2008). Primary enteroid monolayers retain donor-derived differentiation and multilineage diversity but require validation to confirm they form a functional epithelial

barrier. Tight junction organization and barrier function were therefore characterized prior to BAC exposure.

3.1.1 Tight Junction Protein Localization in Enteroid Monolayers

To assess tight junction architecture, immunocytochemical (ICC) staining was performed on confluent enteroid monolayers derived from one donor (HDO07; Table 2.1) for ZO-3, a cytoplasmic scaffolding protein, and occludin, a transmembrane tight junction component. Confocal microscopy revealed uniform junctional localization of both proteins, with continuous staining at cell-cell contacts across the monolayer surface (Figure 3.1.1A, B). Orthogonal views showed ZO-3 concentrated apically relative to Hoechst-stained nuclei, consistent with its position at the apical junctional complex (Figure 3.1.1C). Occludin was distributed across both apical and lateral membranes without a discrete apical band, consistent with its behavior as a transmembrane protein that extends along the lateral membrane (Figure 3.1.1D). The contrasting distributions match the distinct roles of the two proteins in junctional organization. Together, the localization of both proteins indicates that enteroid monolayers form organized, polarized tight junctions consistent with those of intestinal epithelium. Additional staining for the efflux transporter MRP3 and the proliferative marker Ki-67 was performed and is presented in Supplementary Figure 2.

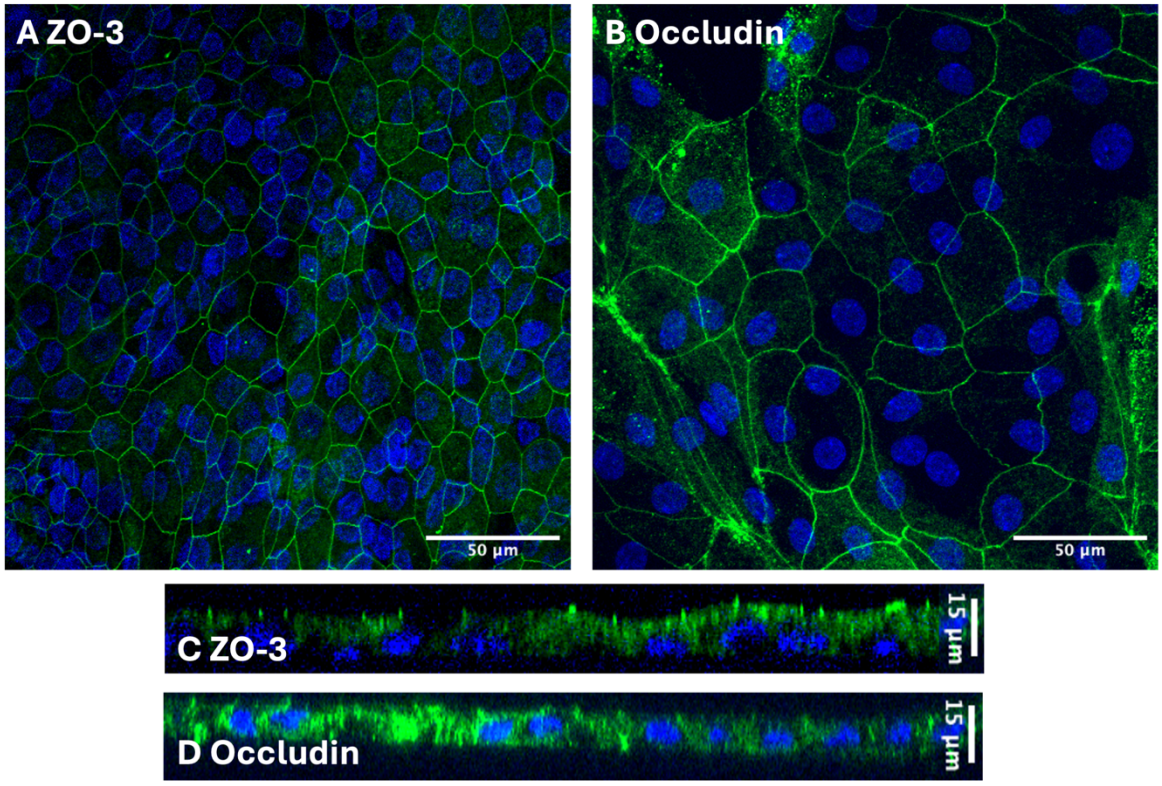

Figure 3.1.1 Tight junction protein localization in human enteroid monolayers. ICC staining of ZO-3 **[A, C]** and occludin **[B, D]** in enteroid monolayers derived from a single donor. XY confocal images **[A, B]** demonstrate uniform intercellular junctional organization of both proteins across the monolayer surface (green), acquired at 60x magnification with a water immersion objective. **[C]** Orthogonal image verifies ZO-3 apical localization relative to Hoechst-stained nuclei (blue). **[D]** Orthogonal view confirms apical and lateral placement of occludin without distinct membrane polarization (green), relative to Hoechst-stain nuclei (blue). Scale bars: 50 µm **[A, B]**; 15 µm **[C, D].**

3.1.2 Enteroid Monolayers Develop Robust and Stable TEER

Once the monolayers became visually confluent, TEER was measured prior to media changes every two days from Day 6 to Day 14 of differentiation. All three donors (Table 2.1) developed measurable resistance by Day 6, with mean values ranging from approximately 1000-1230 Ω•cm^2 at this earliest timepoint (Figure 3.1.2). The cross-donor mean rose to a plateau near 1350 Ω•cm^2 through Days 8-12, with peak values exceeding 1700 Ω•cm^2. Resistance declined modestly by Day 14, with a cross-donor mean of approximately 1055 Ω•cm^2, reflecting inter-

donor variation across the differentiation window rather than barrier loss. At the experiment timepoint of Day 14, all monolayers maintained TEER well above the 100 Ω•cm² threshold for intact epithelial barrier function and substantially above blank insert controls, confirming barrier integrity at the time of BAC exposure. The development of resistance well above this threshold across three independent donors demonstrates that enteroid monolayers reliably form a functional epithelial barrier under the differentiation conditions employed.

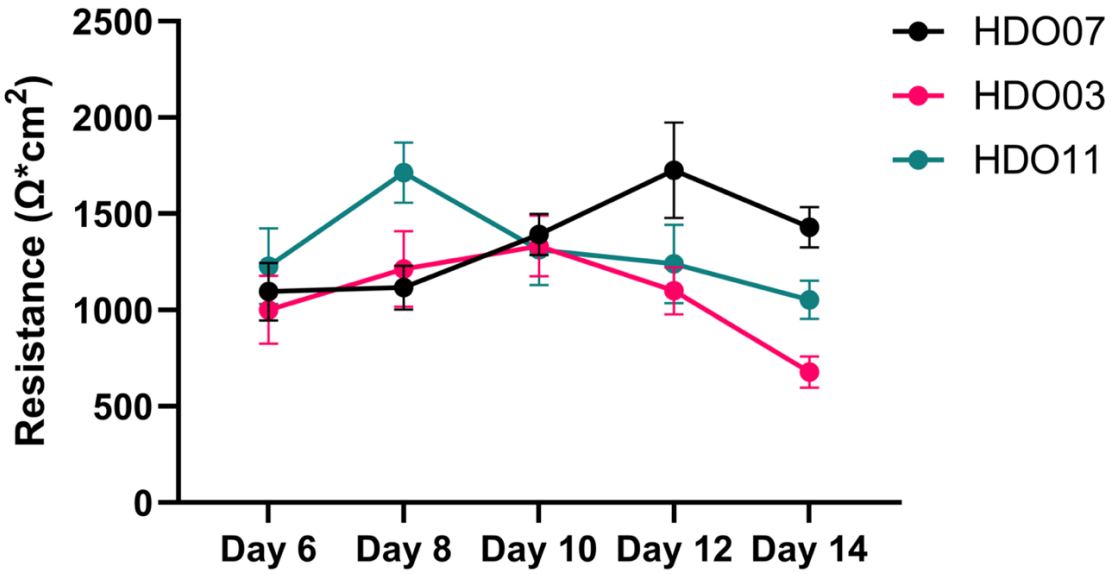

Figure 3.1.2 Transepithelial electrical resistance of enteroid monolayers across three independent donors over the differentiation period. TEER was measured prior to media changes every two days from Day 6 through Day 14 post-seeding. Raw resistance values were blank-subtracted and normalized to Transwell surface area (0.33 cm²). Data points represent mean ± SD of 40 technical replicates across three independent donors.

3.1.3 Enteroid Monolayers Restrict Paracellular Permeability to Lucifer Yellow

Paracellular permeability was assessed on Day 14 of differentiation using lucifer yellow (LY), a membrane-impermeant fluorescent tracer, applied in both apical-to-basolateral (A→B) and basolateral-to-apical (B→A) directions. Enteroid monolayers exhibited low percent diffusion in both directions across all three donors, with mean A→B values ranging from 0.15-0.61% and mean B→A values ranging from 0.04-0.23% (Figure 3.1.3). Cell-free blanks with collagen IV-

coated Transwell inserts showed substantially higher diffusion, with mean A→B values of approximately 12-14% across all donors, confirming that the restricted permeability observed in monolayers reflects an intact epithelial barrier. Mean B→A diffusion in blank inserts was lower than A→B (~4.5%), consistent with the differing donor and receiver chamber volumes between directions rather than any directional barrier property, and remained significantly higher than diffusion across monolayers ($p < 0.0001$, one-way ANOVA with Dunnett's post-hoc test). The uniformly low paracellular flux observed across all three donors demonstrates that enteroid monolayers maintain a selectively permeable barrier after 14 days of differentiation, supporting their suitability as a physiologically relevant model for toxicology studies.

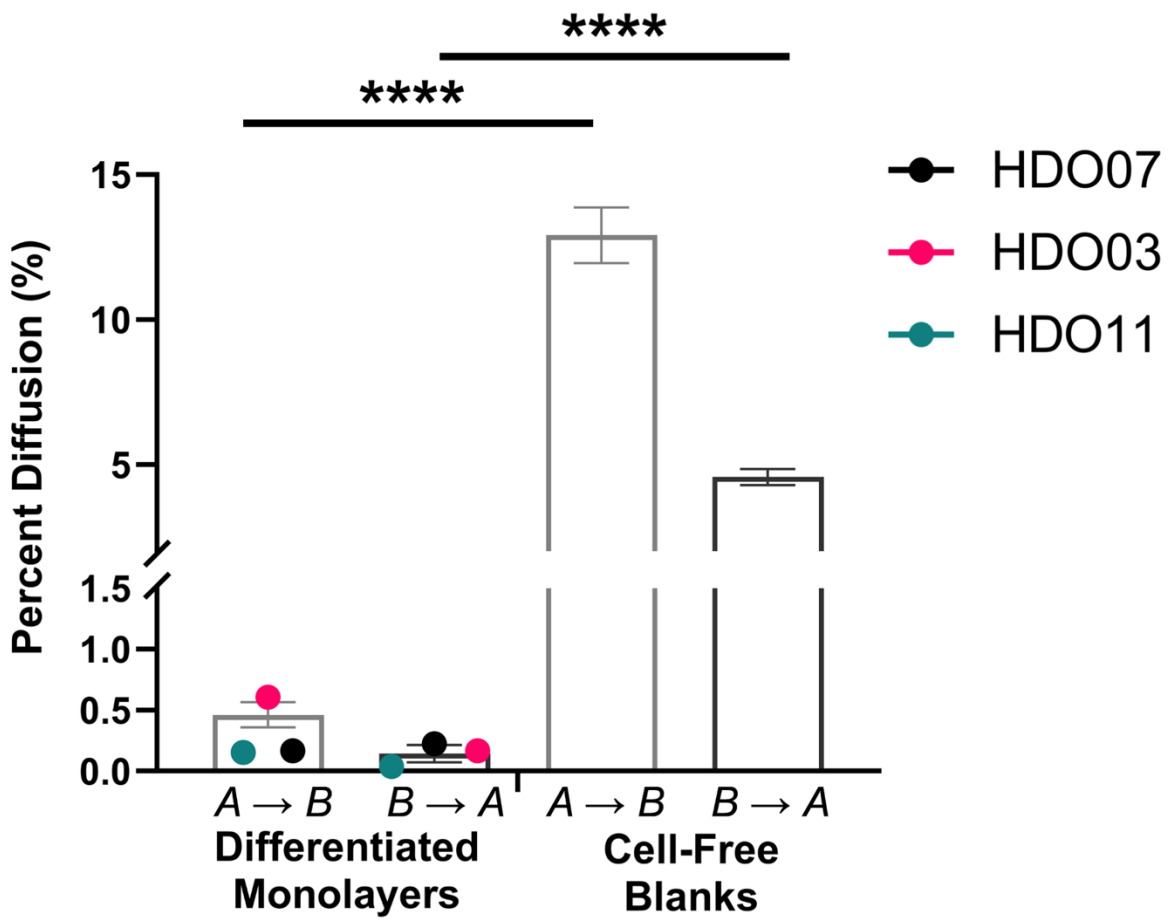

Figure 3.1.3 Enteroid monolayers restrict paracellular permeability to lucifer yellow. Percent diffusion of lucifer yellow (10 μM) was assessed on Day 14 of differentiation in the apical-to-basolateral (A→B) and basolateral-to-apical (B→A) directions. Cell-free blanks contained collagen IV-coated inserts without monolayers. Bars represent mean ± SD of 40 technical replicates across three independent donors (HDO07, HDO03, HDO11). **** $p < 0.0001$, one-way ANOVA with Dunnett's post-hoc test.

3.2 Acute BAC Exposure Elicits a Coordinated Transcriptional Response in Human Enteroid Monolayers

To characterize the transcriptional response of the small intestine upon acute BAC exposure, enteroid monolayers derived from three independent donors (Table 2.1) were exposed apically to a BAC cocktail (50 nM, 500 nM, or 3 μM) or a vehicle control for 16 hours. After this incubation period, RNA-seq was performed as described in Section 2.9. Initial transcriptomic analysis of a pilot donor revealed that all three BAC concentrations produced broadly similar transcriptional profiles, with treated samples clustering together and away from vehicle controls, suggesting that the transcriptional response was already maximal or near-maximal at concentrations as low as 50 nM (Supplementary Figure 3). Based on this finding, subsequent sequencing of the remaining two donors was conducted at 3 μM only, still capturing the maximal response. Across the three donors, BAC exposure elicited a robust and predominantly upregulated transcriptional response in two donors (HDO07 and HDO11), while the third (HDO03) showed no detectable differential expression. The two responding donors differed in both the magnitude and breadth of differential gene expression (Figure 3.2.1). The following subsections characterize the convergent transcriptional signatures across responding donors and describe the functional gene programs implicated in the response to 16-hour BAC exposure.

3.2.1 Multi-donor RNA-seq Reveals a Convergent Transcriptional Response with Inter-donor Variability

Upon exposure to a 3 μM BAC cocktail, the transcriptional response between the two responding donors (HDO11 and HDO07) differed substantially in magnitude. HDO11 produced 1,349 differentially expressed genes (DEGs), while HDO07 produced 355, with both donors exhibiting a predominantly upregulated response; HDO03 yielded no detectable DEGs under the same conditions (Figure 3.2.2). Comparison of DEG lists across donors revealed limited overlap, with 64 genes shared between the two donors (Figure 3.2.2 A; Supplementary Table 2). This pattern indicates that while both donors mount a transcriptional response of similar directionality, the quantity and specific gene targets differ considerably between individuals. However, only 15 of the 64 overlapping genes changed in the same direction across both donors (Supplementary Table 2), with the remainder regulated in opposite directions. The concordant upregulated genes included the proliferation-associated *CDCA7*, *DBF4*, and *WDR5*. The downregulated set included growth-suppressive and barrier-associated genes such as *IGFBP3*, *RASSF6*, and *MUC3A*.

Pathway-level analysis reinforced this pattern of donor variability alongside a conserved core response. iPathwayGuide analysis identified 71 significantly enriched pathways in HDO11 and 78 in HDO07 (FDR < 0.05), with only 10 pathways shared between donors (Figure 3.2.2 B). Notably, these shared pathways include cell cycle, p53 signaling, PI3K-Akt signaling, and FoxO signaling, pointing to a proliferative and stress-related transcriptional program elicited by acute BAC exposure regardless of donor background. The donor-specific pathways likely reflect interindividual variability rather than qualitatively distinct toxicodynamic responses.

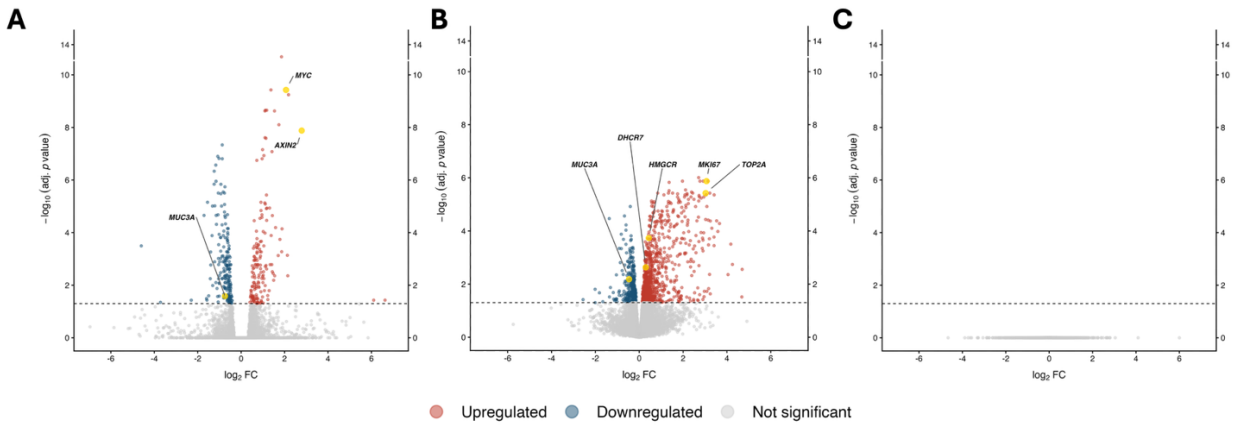

Figure 3.2.1. Volcano plots of DEGs following 16-hour BAC exposure across three independent donors. Each panel displays the transcriptional response of a single donor (**A**: HDO07, **B**: HDO11, **C**: HDO03) to a 3 µM BAC cocktail relative to vehicle control. Each point represents a gene, plotted by log_2 fold change (x-axis) against -log10 adjusted p-value (y-axis). Upregulated genes are shown in red, downregulated in blue, and non-significant genes in gray. Dashed lines indicate thresholds for significance (FDR < 0.05). HDO03 produced no significant differentially expressed genes.

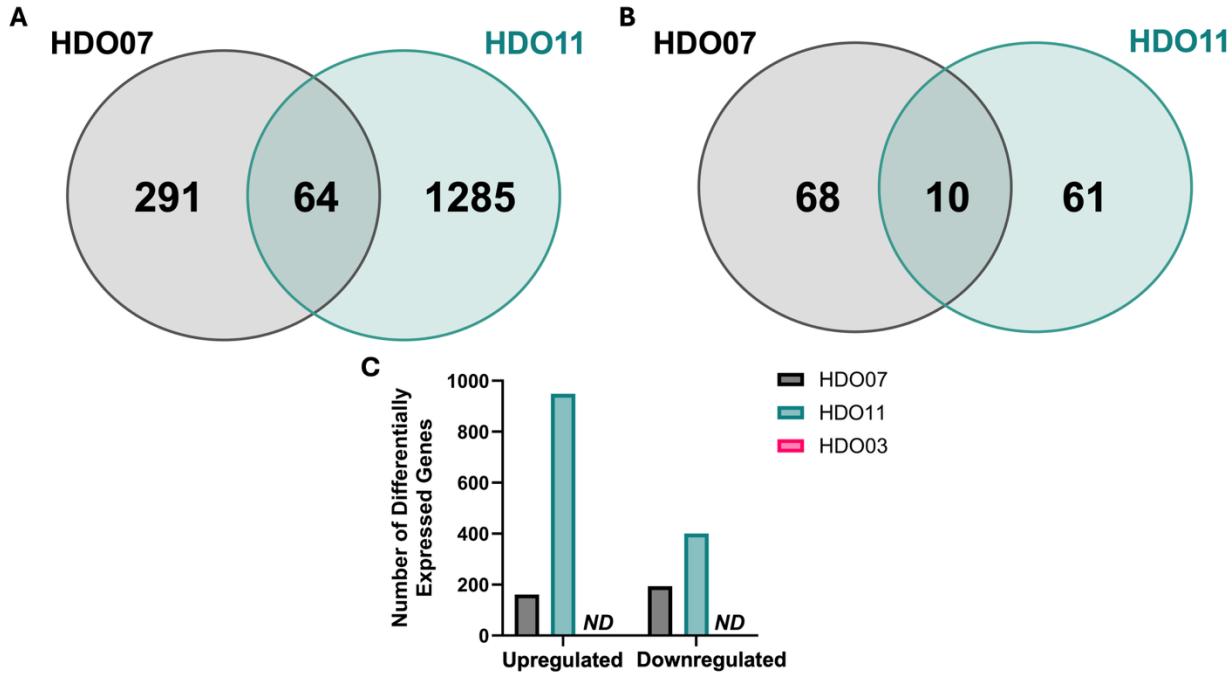

Figure 3.2.2. Multi-donor comparison of DEGs and enriched pathways following 16-hour BAC exposure. [A] Venn diagram showing overlap of significant DEGs (FDR < 0.05) between HDO07 and HDO11 at the 3 µM BAC treatment compared to vehicle control. **[B]** Venn diagram showing overlap of significantly enriched pathways (FDR < 0.05) between HDO07 and HDO11. **[C]** Bar chart showing the total number of upregulated and downregulated DEGs per donor. ND indicates no significant differential gene expression.

3.2.2 BACs Induce a Coordinated Cell Cycle and Proliferative Gene Expression Program

Despite substantial inter-individual differences upon BAC exposure, both HDO07 and HDO11 showed significant changes in cell cycle and DNA replication pathways following acute 3 μM BAC exposure. These pathways were among the ten shared between donors (Figure 3.2.2B), and in both cases the enrichment was driven predominantly by upregulated genes, consistent with a pro-proliferative response independent of donor variability in DEG magnitude.

In HDO11, this pathway-level enrichment was reflected in the upregulation of many individual cell cycle and DNA replication genes (Figure 3.2.3). Among these were the mitotic kinases *CDK1, AURKB*, *PLK1*, and *TTK*, and cyclins spanning both G1/S and G2/M phases, including *CCNE1, CCNE2*, *CCNA2*, *CCNB1*, and *CCNB2*. Both *E2F1* and *E2F2*, transcription factors driving S-phase progression, were upregulated. Replication-specific genes were also induced, with *MCM2* through *MCM7, ORC1, ORC6, CDC6, CDT1*, and *PCNA* all showing increased expression (Figure 3.2.3). With the single exception of *EP300*, every differentially expressed cell cycle gene in HDO11 was upregulated, pointing to a sweeping and largely unidirectional activation of the cell cycle and DNA replication in this donor.

In HDO07, the picture was different but pointed in the same direction. Rather than broad induction of downstream effectors, HDO07 showed upregulation of genes earlier in the proliferative cascade (Supplementary Table 3). *MYC* was among the most strongly upregulated genes overall ($\log_2$FC = 2.07), alongside *CDC25A*, *CDT1*, *CDK6*, and *DBF4*. At the same time, the cyclin-dependent kinase (CDK) inhibitors *CDKN1A* and *CDKN2B* were downregulated along with *GADD45A*, indicating release of negative regulators of cell cycle progression (Supplementary Table 3). PI3K-Akt and canonical Wnt signaling pathways were enriched in this

donor while TGF-β pathway genes were suppressed, which fits with a cellular environment being pushed toward growth and away from quiescence (Supplementary Figure 4; Supplementary Table 3). MYC sits downstream of both PI3K-Akt and canonical Wnt signaling and upstream of the replication factors that dominated the HDO11 response, positioning it as a candidate node linking the two donor programs.

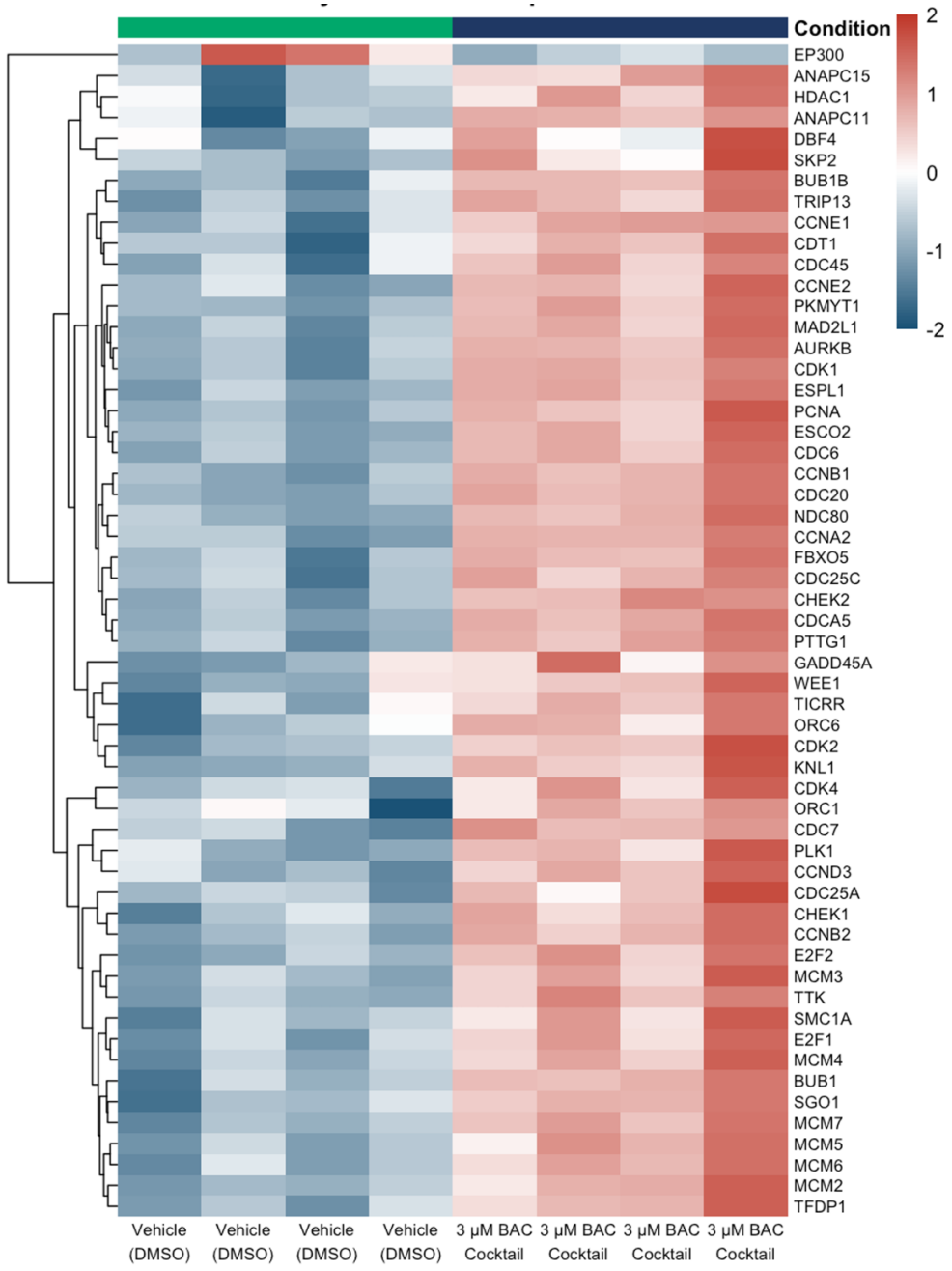

Figure 3.2.3 BAC Exposure induces upregulation of cell cycle genes. Heatmap displaying normalized expression of differentially expressed cell cycle genes following 16-hour exposure to 3 μM BAC cocktail relative to vehicle control with DMSO (n = 1 donor, HDO11). Each column represents a technical replicate (n = 4) Genes are clustered hierarchically by expression pattern. Color scale represents $\log_2$ counts per million (logCPM), with red indicating higher expression and blue indicating lower expression relative to the row mean. Differentially expressed genes were identified with a threshold of FDR < 0.05.

3.2.3 Acute BAC Exposure Alters Cholesterol and Lipid Metabolic Gene Expression

Pathway analysis of the HDO11 acute transcriptional response to 3 μM BAC exposure revealed significant enrichment of lipid metabolic processes. Among these pathways, steroid biosynthesis was the most significantly enriched, followed by fatty acid metabolism, biosynthesis of unsaturated fatty acids, fatty acid degradation, fatty acid elongation, fat digestion and absorption, glycerolipid metabolism, and steroid hormone biosynthesis (Figure 3.2.4). Together these findings indicate that acute BAC exposure broadly disrupts lipid metabolic gene expression in the duodenal epithelium, spanning membrane lipid synthesis, fatty acid processing, and lipid absorption.

Within the steroid biosynthesis pathway, genes spanning the mevalonate-to-cholesterol arc were upregulated. Rate-limiting enzymes at the beginning of the pathway including *HMGCS1* and *HMGCR* were upregulated alongside *MVK, MVD, FDPS, FDFT1*, *SQLE*, and *LSS*, which encode the enzymes converting acetyl-CoA to lanosterol (Figure 3.2.5; Supplementary Table 4). Further downstream, *DHCR7* and *DHCR24*, which catalyze the final steps to cholesterol, were also upregulated (Figure 3.2.5; Supplementary Table 4). Genes mediating cholesterol sensing and uptake were also upregulated, including the SREBP2 targets *LDLR*, *PCSK9*, *INSIG1* and *INSIG2* (Supplementary Table 4), alongside downregulation of the efflux transporter *ABCA1* (Figure 3.2.5; Supplementary Table 4). Enrichment of fatty acid metabolism pathways adds a dimension to this lipid response. Upregulation of genes involved in

fatty acid elongation and biosynthesis of unsaturated fatty acids suggests membrane composition remodeling (Supplementary Table 4). Genes contributing to fatty acid degradation and fatty acid metabolism were also enriched. A complete list of differentially expressed genes across all lipid homeostasis pathways is provided in Supplementary Table 4.

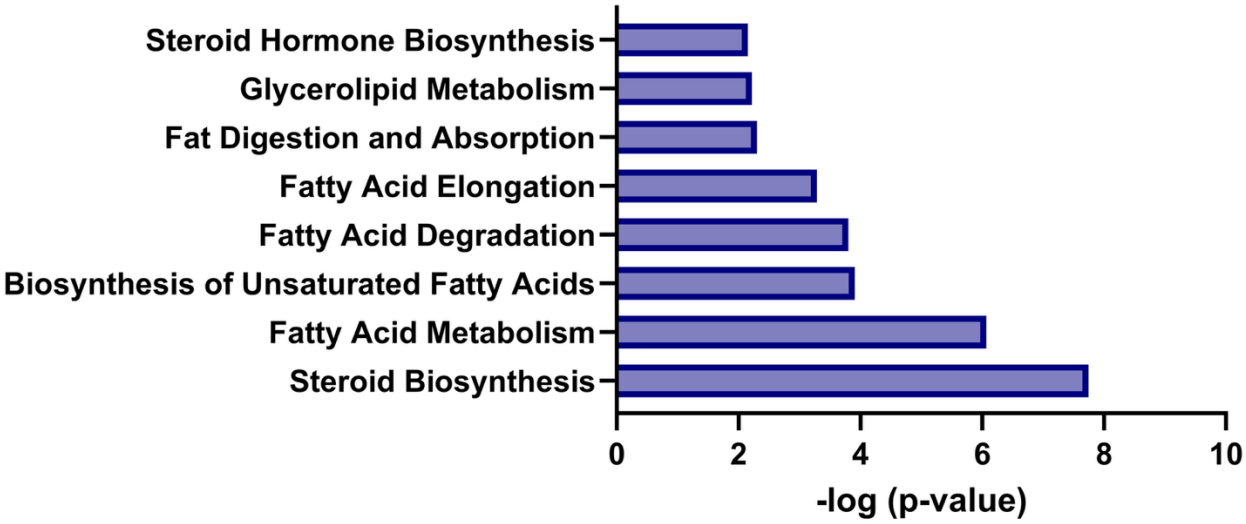

Figure 3.2.4. Significantly enriched pathways involved in lipid homeostasis. Bar chart displaying significantly enriched lipid-related pathways identified by iPathwayGuide pathway analysis following 16-hour exposure to 3 µM BAC cocktail relative to vehicle control (n = 1 donor, HDO11). Pathways are ranked by statistical significance and displayed as negative log-transformed corrected p-values. Only pathways with FDR < 0.05 are shown.

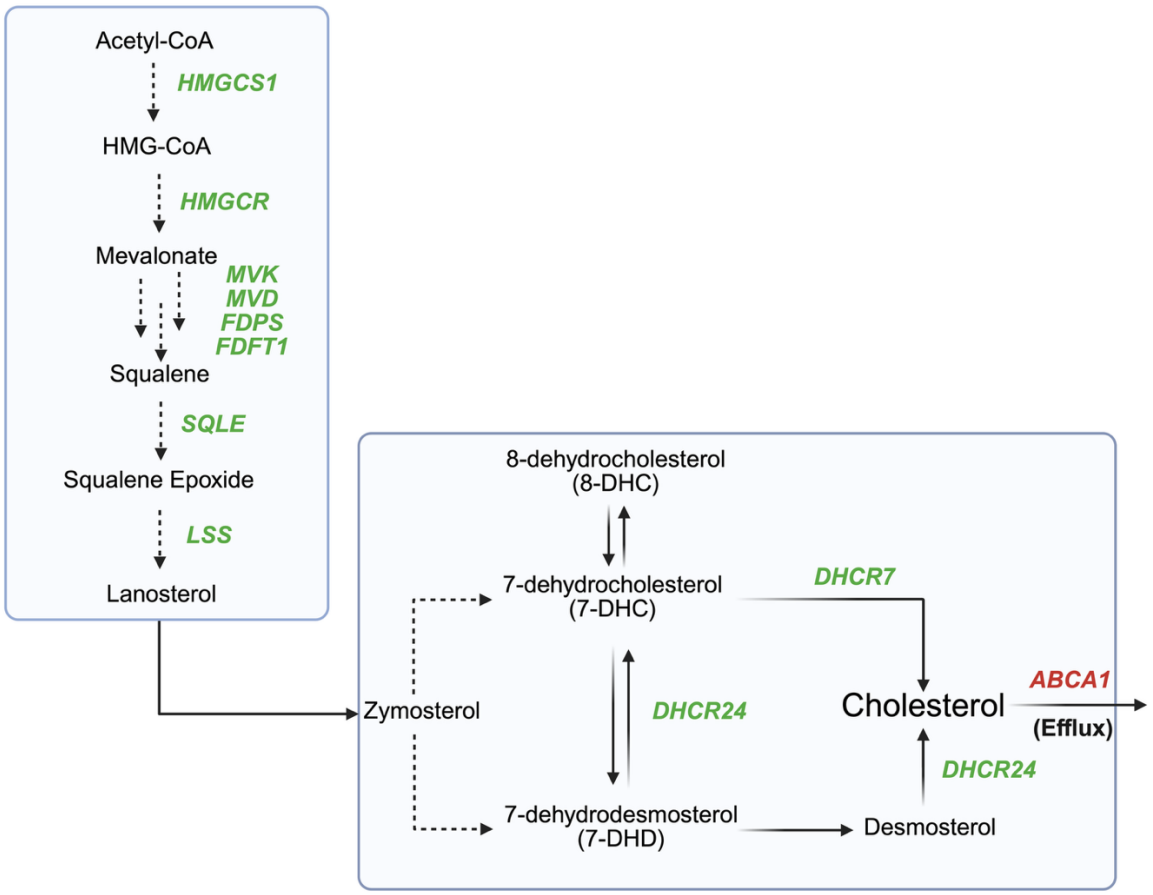

Figure 3.2.5. Acute BAC exposure induces transcriptional upregulation of the cholesterol biosynthetic pathway. Schematic of the cholesterol biosynthesis pathway depicting differentially expressed genes following 16-hour exposure to 3 µM BAC cocktail relative to vehicle control (n = 1 donor, HDO11). Gene symbols in green indicate upregulation and red indicates downregulation. Dashed arrows represent multi-step reactions. Differentially expressed genes were identified with a threshold of FDR < 0.05.

3.2.4 BACs Elicit Induction of Xenobiotic Metabolism and Transport Genes

Beyond cell cycle and lipid homeostasis pathways, acute BAC exposure induced broad transcriptional changes in drug-metabolizing enzymes and transporters (DMET), suggesting the duodenal epithelium mounted a xenobiotic response. Phase I oxidative metabolism genes were among the most consistently altered, including upregulation of *CYP4F12*, which has been shown to directly metabolize BAC compounds (Seguin et al., 2019), alongside *CYP51A1* (Supplementary Table 4), aldo-keto reductases including *AKR1C4*, and the antioxidant enzyme

SOD2, while *CYP3A5* was downregulated (Figure 3.2.6A). The downregulation of *CYP3A5* is notable given its status as the predominant intestinal cytochrome P450 and a major mediator of first-pass xenobiotic metabolism in the small intestine. Phase II conjugation enzymes were also broadly upregulated, including the glutathione S-transferases *GSTA1* and *GSTA2*, the UDP-glucuronosyltransferases *UGT1A1* and *UGT1A10*, and the sulfotransferase *SULT1A3* (Figure 3.2.6B). Of these, *SULT1A3* showed the largest fold change ($log_2FC = 4.68$).

Membrane transporter expression was also altered in HDO11. Among efflux transporters, *SLC30A10* showed the largest upregulation, encoding a zinc and manganese efflux transporter expressed in intestinal epithelium, while *ABCA1* was downregulated consistent with the cholesterol retention response described in section 3.2.3 (Figure 3.2.6C; Figure 3.2.5). Among uptake transporters, *SLC6A4*, encoding the serotonin reuptake transporter SERT, showed the highest fold change in this category, alongside upregulation of the fatty acid transporter *SLC27A3* and the amino acid transporter *SLC1A4* (Figure 3.2.6 D). Of particular interest, *SLC6A4* was upregulated in HDO11 while *SLC19A3*, encoding the thiamine transporter ThTR2, was downregulated in HDO07 (Supplementary Table 5). Whether these transcriptional changes reflect compensatory responses to BAC-mediated transporter inhibition remains to be determined.

In contrast to the broad DMET induction observed in HDO11, HDO07 did not show a comparably robust Phase I/II xenobiotic metabolism response, with the acute transcriptional changes in that donor weighted more toward transporter gene alterations than coordinated drug metabolizing enzyme upregulation. A complete list of differentially expressed DMET genes from all donors is provided in Supplementary Table 5.

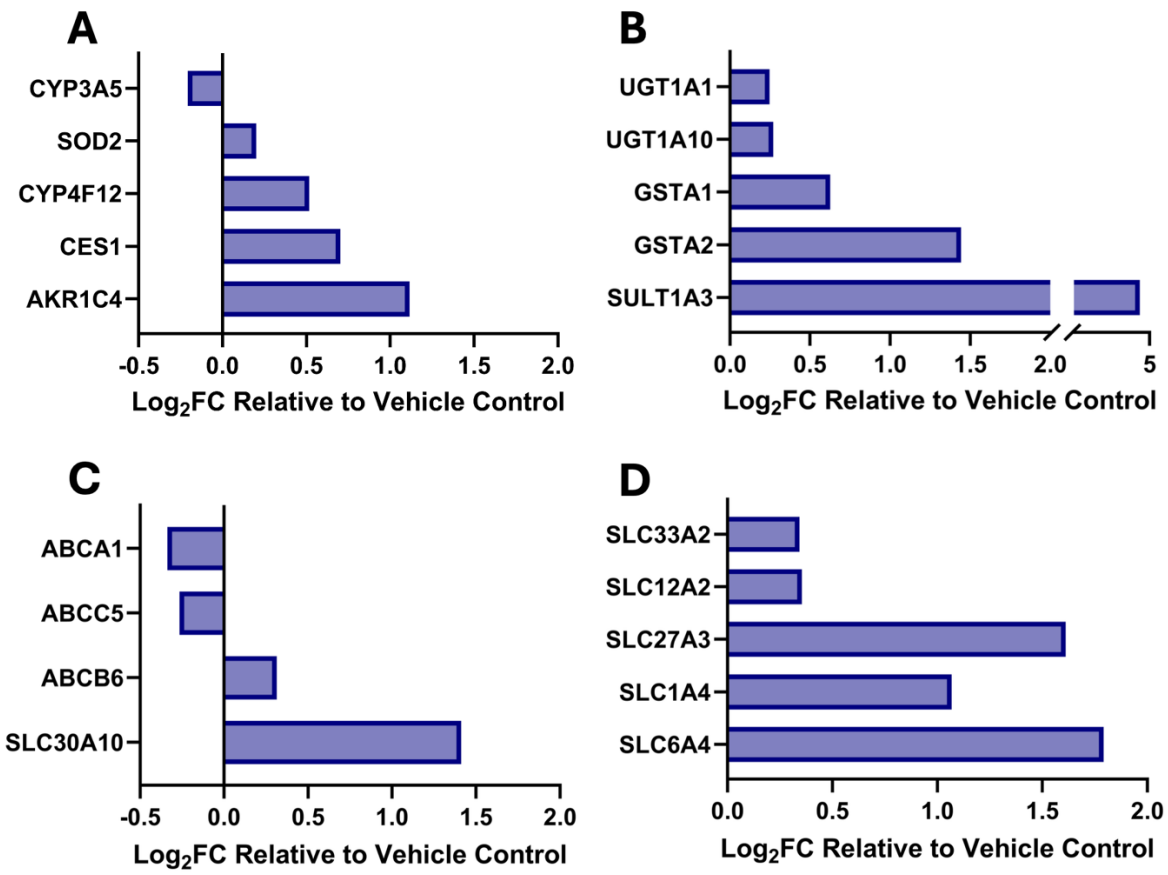

Figure 3.2.6. Selected differentially expressed DMETs upon BAC treatment. Bar charts displaying $\log_2$ fold change of differentially expressed DMET genes following 16-hour exposure to 3 µM BAC cocktail relative to vehicle control (n = 1 donor, HDO11). **[A]** Phase I metabolism genes. **[B]** Phase II conjugation genes. **[C]** Efflux transporter genes. **[D]** Uptake transporters genes. Axis break in panel B indicates discontinuous scale for *SULT1A3*. Differentially expressed genes were identified with a threshold of FDR < 0.05.

3.3 Human Enteroid Monolayers Adapt to Chronic BAC Exposure Without Significant Barrier Dysfunction

An advantage of human enteroid monolayers is that they can be viable for weeks at a time. This extended culture time allowed for assessing the effects of chronic exposure to three concentrations of the same BAC cocktail (Figure 2.1; 50 nM, 500 nM, or 3 µM) or vehicle control on the intestinal epithelium. These exposure scenarios are relevant to occupational settings where individuals may encounter these compounds repeatedly over extended periods.

Chronic BAC exposure was assessed using one donor (HDO07; Table 2.1), with changes in gene expression, TEER, and lucifer yellow (LY) permeability evaluated across BAC-treated and vehicle control conditions. Treatment timepoints and monolayer maintenance for chronic BAC exposures are detailed in section 2.4.

3.3.1 RNA-seq Reveals Minimal Transcriptional Changes Under Chronic BAC Exposure

To assess the transcriptional response to chronic BAC exposure, enteroid monolayers were dosed apically every two days with the BAC cocktail at 50 nM, 500 nM, 3 μM, or vehicle (DMSO) diluted in ODM, beginning on Day 8 post-seeding. Monolayers were collected after 16 days of exposure (Day 24 of differentiation) for bulk RNA-seq. Differential expression analysis using a significant threshold of FDR < 0.10 identified 10 DEGs at 3 μM relative to vehicle, with no significant DEGs detected at 50 nM or 500 nM. Of the 10 DEGs, 9 were upregulated, and one, *BCL2L2-PABPN1*, was downregulated (Figure 3.3.1A).

Although no canonical signaling pathways were significantly enriched (FDR < 0.05) in iPathwayGuide impact analysis, gene ontology (GO) biological process analysis identified significant overrepresentation of microvillus organization terms (Figure 3.3.1B). This includes regulation of microvilli length, microvilli organization, and regulation of cell projection size ($p < 0.05$), driven by the coordinated upregulation of genes encoding *CDHR5* and *VIL1*. Consistent with a differentiation or surface remodeling response rather than cellular stress or damage, four of the nine upregulated DEGs (*KRT20*, *VIL1*, *CDHR5*, and *SLC17A4*) encode proteins with established roles at the intestinal brush border. Additionally, negative regulation of triglyceride catabolism was identified as an enriched GO term. These results differ markedly from the acute transcriptional response in the same donor, which was characterized by coordinated activation of

proliferative and stress-response programs including PI3K-Akt signaling, canonical Wnt signaling and cell cycle activation.

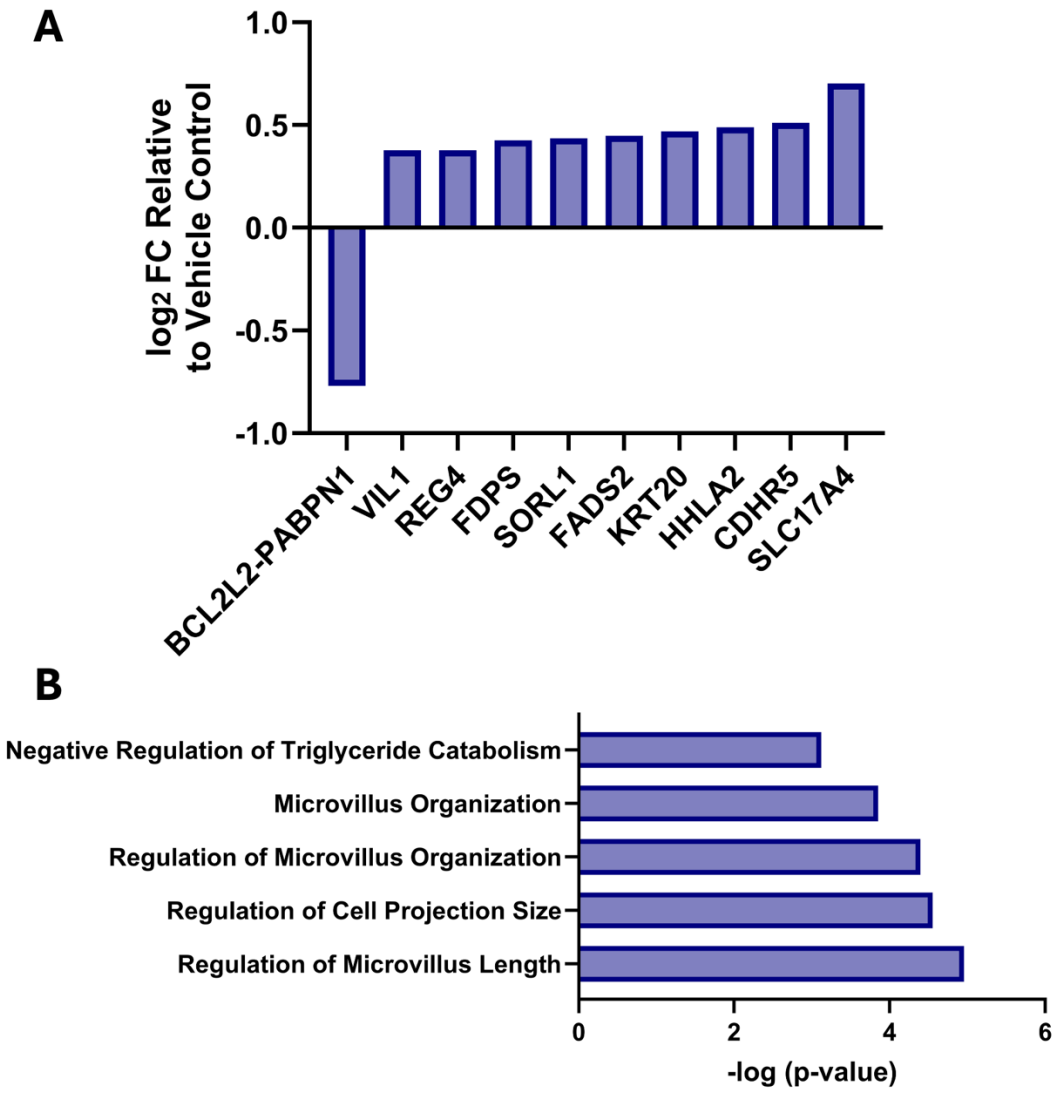

Figure 3.3.1. Transcriptional response to chronic BAC cocktail exposure in enteroid monolayers. [A] Log_2 fold change of the 10 DEGs identified following chronic exposure to 3 µM BAC cocktail relative to vehicle control (n = 1 donor, HDO07; FDR < 0.10). **[B]** Top 5 enriched GO Biological Process terms associated with the chronic DEG set, ranked by -log(p-value).

3.3.2 Chronic BAC Exposure Does Not Alter Epithelial Barrier Integrity at Physiologically Relevant Concentrations

To evaluate whether repeated luminal BAC exposure disrupted paracellular barrier integrity, LY permeability assays were performed at three timepoints: prior to BAC exposure (Day 8 of differentiation), after one week of exposure (Day 16 of differentiation), and at the end of the two-week exposure period (Day 24 of differentiation). Additionally, TEER was monitored every two days prior to media changes throughout this time course.

Prior to BAC treatment, untreated HDO07 enteroid monolayers exhibited a mean LY diffusion of 0.181% ± 0.030%, compared to 12.2% ± 0.575% in cell-free blank inserts, confirming intact barrier function at baseline (Figure 3.3.2 A). After one week of BAC exposure, LY diffusion remained low and comparable across all concentrations (50 nM: 0.593% ± 0.131%; 500 nM: 0.591% ± 0.175%; 3 μM: 0.619% ± 0.071%; vehicle: 0.567% ± 0.044%), with cell-free blanks showing 17.1% ± 0.365% diffusion (Figure 3.3.2 B). At the end of the two-week exposure period, LY diffusion remained similarly low across all conditions (50 nM: 0.504% ± 0.143%; 500 nM: 0.627% ± 0.046%; 3 μM: 0.430% ± 0.075%; vehicle: 0.388% ± 0.069%), with cell-free blanks at 18.4% ± 0.298% (Figure 3.3.2 C). Longitudinal tracking across all three timepoints revealed no increase in paracellular permeability under any BAC concentration, with a modest convergence toward lower values across most conditions, apart from 500 nM BAC (Figure 3.3.2 D). Notably, the 500 nM BAC cocktail was the only condition with a net increase in LY permeability over the second week of exposure (Figure 3.3.2 D). TEER was similarly maintained above 1000 $\Omega \cdot cm^2$ in all conditions throughout the two-week exposure period, with no sustained change in resistance in BAC-treated wells relative to DMSO vehicle (Supplementary Figure 5). Together, these data indicate that chronic luminal BAC exposure at 50 nM, 500 nM, or 3 μM does not significantly compromise epithelial barrier integrity over a two-week treatment period.

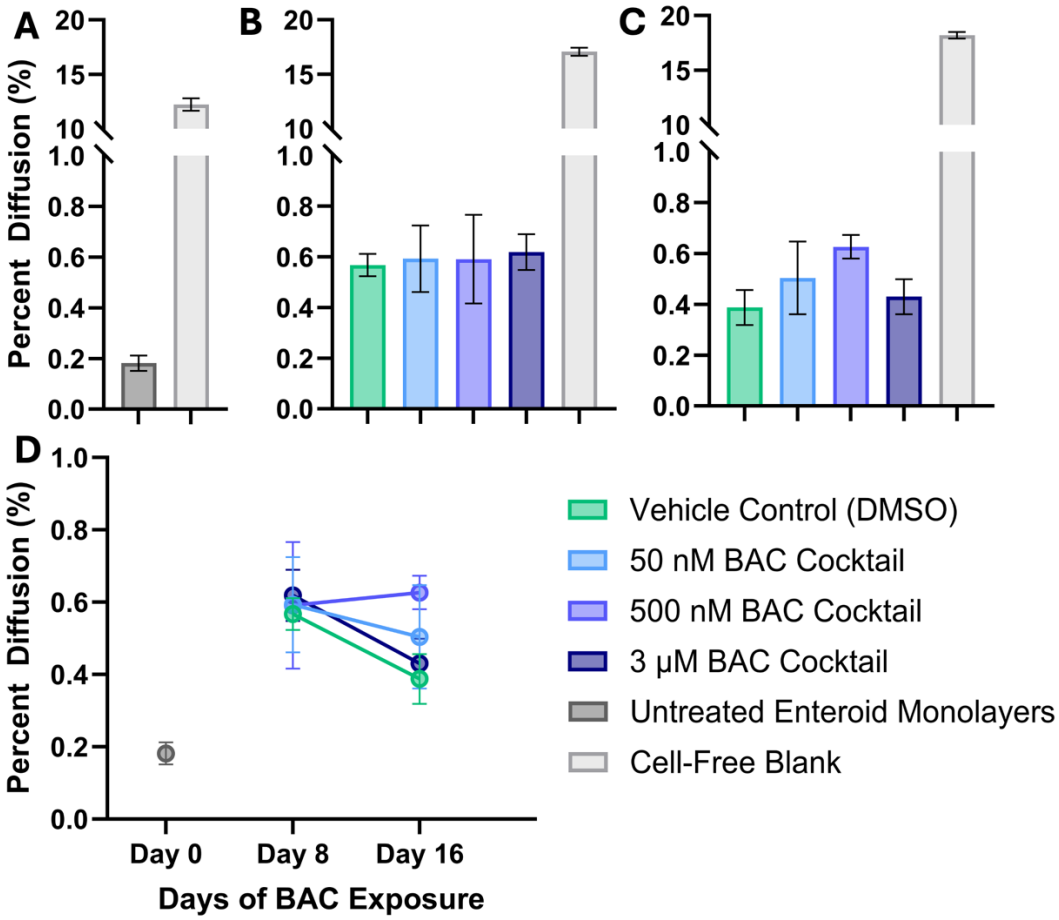

Figure 3.3.2 Lucifer yellow permeability is maintained in enteroid monolayers throughout chronic BAC exposure. [A] LY Percent diffusion in untreated enteroid monolayers prior to BAC exposure (Day 0 of exposure, Day 8 of differentiation). **[B]** LY percent diffusion following one week of exposure to a BAC cocktail or vehicle control (one week of exposure, Day 16 of differentiation). **[C]** LY percent diffusion following two weeks of exposure to a BAC cocktail or vehicle control (two weeks of exposure, Day 24 of differentiation). **[D]** Longitudinal LY percent diffusion across all three timepoints for each treatment condition. In all panels, cell-free blank inserts coated with collagen IV are shown as a reference for maximal diffusion in the absence of an epithelial barrier. Data represents mean ± SD; n = 4 technical replicates per condition from a single donor experiment (HDO07; 1 biological replicate).

4. Discussion

Primary human duodenal enteroid monolayers mount a robust transcriptional response to a 16-hour BAC cocktail exposure, characterized by upregulation of cell cycle progression, cholesterol biosynthesis, and xenobiotic metabolism genes in two of three donors. In contrast,

chronic repeated dosing over 16 days produced minimal transcriptional disruption and no significant change in barrier integrity, suggesting adaptation rather than cumulative injury.

Validation of the enteroid monolayer system prior to BAC exposure confirmed that the model was suitable for toxicological dosing. Tight junction architecture, barrier resistance, and paracellular permeability were each consistent with prior characterizations of this model (Arian et al., 2025), indicating monolayers had reached a differentiated, physiologically relevant state by Day 14 (Figures 3.1.1-3.1.3). Detection of MRP3 established retention of intestinal transporter expression in differentiated monolayers (Supplementary Figure 2A), consistent with the DMET gene expression observed in the acute transcriptional response and supporting the functional relevance of the xenobiotic metabolism findings described below. ICC staining for Ki-67 at baseline revealed sparse proliferative activity in vehicle-treated monolayers, indicating that the epithelium was predominantly quiescent at the time of acute BAC exposure (Supplementary Figure 2B). This baseline is consequential for interpreting the acute transcriptional response: the pro-proliferative gene program elicited by BAC occurred against a background of low endogenous proliferation, suggesting it reflects a compound-driven alteration rather than an artifact of a highly mitotic baseline state. Previous studies on enteroid monolayers similarly report culture conditions that support minimal growth and extensive differentiation (Arian et al., 2025). A qualitative increase in Ki-67-positive cells was also observed in monolayers exposed to 500 nM BAC cocktail (Supplementary Figure 2C), providing preliminary protein-level data for the transcriptional proliferative signal, though confirmation across donors and timepoints is needed.

These findings also underscore the advantages of primary enteroid monolayers over other *in vitro* models such as Caco-2 cells or iPSC-derived enteroids for intestinal toxicology. Caco-2 cells are derived from colorectal adenocarcinoma and represent a transformed, homogeneous population that incompletely models the cellular diversity and transporter expression of the native small intestine (Jeong et al., 2025; Sun et al., 2008). Additionally, current differentiation protocols for iPSC-derived enteroid monolayers retain a fetal transcriptional signature inherent to pluripotent stem cell origin that inaccurately reflects adult intestinal gene expression (Bonneau et al., 2025; Kraiczy et al., 2019). By contrast, primary duodenal enteroid monolayers preserve donor-specific biology and multicellular composition, which matters for environmental toxicants, where inter-individual susceptibility is central to risk characterization. The Transwell format further permits direct apical dosing and simultaneous barrier assessment. These factors support the application of this model within a new approach methodology (NAM) framework as a human-relevant alternative for intestinal toxicology, aligning with the principles of the 3Rs by replacing animal-based models with a primary human system.

Prior evidence of BAC-mediated intestinal injury has come predominantly from models with limited translational relevance to human intestinal physiology. These studies have demonstrated structural damage including villus impairment, goblet cell depletion, and upregulation of claudin-2 following oral BAC exposure (Feng et al., 2025; Sanidad et al., 2018). Additionally, *in vivo* BAC exposure has been associated with increased cell proliferation and suppressed apoptosis in colorectal tissue and disruption of gut microbial communities, suggesting BAC bioactivity extends beyond the intestinal epithelium (Lopez et al., 2024; Sanidad et al., 2018). The enzymes responsible for BAC oxidative metabolism, including CYP4F12, CYP4F2, and CYP2D6, are expressed at substantially lower levels in the intestinal

epithelium relative to the liver, where CYP3A accounts for the majority of total P450 activity (Seguin et al., 2019; Xie et al., 2016). This limited oxidative metabolic capacity suggests that enterocytes may rely less on local CYP-mediated clearance of intracellular BAC, potentially altering exposure dynamics at the site of first contact. However, whether these responses occur in the human intestinal epithelium at physiologically relevant concentrations has remained largely unstudied.

The transcriptomic findings reported here begin to address this gap, showing that acute BAC exposure elicits a proliferative and metabolic response in primary human enteroid monolayers. Initial transcriptomic analysis of HDO07 revealed that all three BAC cocktail concentrations tested (50 nM, 500 nM, and 3 μM) produced broadly similar transcriptional profiles, with treated samples clustering together and away from vehicle controls regardless of concentration (Supplementary Figure 3). The absence of a dose-dependent increase in DEG magnitude across this range suggests that the transcriptional response is already maximal or near-maximal by 50 nM (Supplementary Figure 3). Based on this finding, subsequent sequencing of additional independent donors was conducted at 3 μM only, capturing the maximal transcriptional response. Upon exposure to a 3 μM BAC cocktail, monolayers from two of three donors, HDO07 and HDO11, mounted detectable transcriptional responses of differing magnitude, while HDO03 produced no significant transcriptional changes under the same conditions (Figure 3.2.1; Figure 3.2.2).

The substantial DMET transcriptional changes in HDO11 suggest the duodenal epithelium mounted an active, intestine-specific detoxification program in response to BAC exposure. Most striking was the induction of *SULT1A3* ($\log_2$FC = 4.68; Figure 3.2.6B), the

predominant intestinal sulfotransferase responsible for clearing catecholamines and aromatic xenobiotics, and *UGT1A10* (Figure 3.2.6B), a UDP-glucuronosyltransferase whose expression is largely restricted to the small intestinal epithelium and absent from the liver and kidney (Basit et al., 2020; Oda et al., 2017). This intestine-specific conjugation signature points to a detoxification response that is qualitatively distinct from what would be observed in traditional hepatic models. Upregulation of *CYP4F12* (Figure 3.2.6A), which directly oxidizes BAC along the alkyl chain (Seguin et al., 2019), alongside induction of glutathione S-transferases *GSTA1* and *GSTA2* (Figure 3.2.6B), further reflects a coordinated phase I/II response to BAC exposure. The concurrent downregulation of *CYP3A5* (Figure 3.2.6A), the dominant intestinal cytochrome P450, may reflect substrate competition or transcriptional suppression under acute xenobiotic load and warrants further investigation. Among transporters, previous work has shown that long chain BACs inhibit polyspecific organic cation transporters hOCT1–3 and hMATE1/2-K (Vieira et al., 2024). Given that the serotonin transporter (SERT) and thiamine transporter (ThTr2) are also polyspecific cation transporters, BAC may inhibit them as well. Differential expression of *SLC6A4* (SERT) and *SLC19A3* (ThTr2) across donors (Supplementary Table 5) may reflect inter-donor differences in transporter regulation upon BAC exposure. Moreover, HDO07's DMET response was weighted more toward transporter alterations than phase I/II induction (Supplementary Table 5), possibly reflecting known age-associated variation in intestinal DMET expression given the substantial age difference between donors (27 vs. 70 years; Table 2.1) (Cortreau et al., 2012; Konstandi & Johnson, 2023). These changes were measured at the transcript level, and whether they translate to increased conjugative clearance or compensatory transport activity requires direct metabolite quantification.

Alongside the xenobiotic metabolism response, acute BAC exposure in HDO11 induced upregulation of genes spanning the full cholesterol biosynthetic pathway (Figure 3.2.5), from enzymes *HMGCS1*, *HMGCR*, and *MVD* through the post-squalene steps to *DHCR7* and *DHCR24*, which catalyze the final conversion to cholesterol. This enzymatic induction was accompanied by enrichment of canonical sterol regulatory element-binding protein 2 (SREBP2) target genes *LDLR, PCSK9, INSIG1,* and *INSIG2* (Supplementary Table 4) (Rasmi et al., 2025; Rong et al., 2017). Joint induction of synthesis enzymes and the SREBP2 feedback sensors is the signature of a cell responding to reduced accessible cholesterol (Horton et al., 2002), rather than a direct transcriptional effect of BAC on individual genes. The concurrent downregulation of *ABCA1* (Figure 3.2.5; Supplementary Table 4), which mediates cholesterol efflux from enterocytes (Brunham et al., 2006), is consistent with a program directed toward restoring intracellular cholesterol.

This compensatory response is best understood in the context of the enterocyte's specialized role in cholesterol handling. Unlike hepatocytes, which regulate circulating systemic cholesterol, the intestinal epithelium is oriented towards absorption and trafficking of exogenous cholesterol (Betters & Yu, 2010). Endogenous cholesterol synthesis in the small intestine largely serves as a homeostatic brake, induced when luminal cholesterol uptake is insufficient to meet cellular demand (Davis et al., 2004). The induction of *ACAT2* (Supplementary Table 4) alongside the biosynthetic enzymes further suggests an attempt to maintain the cholesterol esterification and trafficking the enterocyte depends on. Because enterocyte cholesterol metabolism is weighted toward local membrane maintenance and absorption rather than systemic supply, a BAC-driven disruption in the small intestine likely exerts a local effect on epithelial membrane integrity.

The magnitude of these changes was modest, with most genes shifting between 0.2 and 0.8 $\log_2$ fold change (Supplementary Table 4), but their convergence across the full pathway argues against scattered induction from nonspecific stress. Two non-exclusive mechanisms could account for the reduced accessible cholesterol that drives this response. First, BAC directly inhibits DHCR7, the terminal enzyme of cholesterol biosynthesis, producing accumulation of its substrate 7-dehydrocholesterol (7-DHC) (Herron et al., 2016). Enzymatic blockade at this step would lower cholesterol output and trigger a compensatory SREBP2 feedback response (Horton et al., 2002), consistent with the transcriptional induction observed here. The induction of *DHCR7* itself fits this interpretation, reflecting compensation for inhibition of the enzyme rather than increased cholesterol production, though the present transcriptomic data cannot directly confirm 7-DHC accumulation in the cells. Second, the amphiphilic cationic structure of BAC congeners allows them to intercalate into and destabilize phospholipid bilayers and perturb membrane cholesterol (Kanno et al., 2023); because SREBP2 responds to ER membrane cholesterol levels (Yan et al., 2021), this physical disruption could activate the same feedback loop independently of DHCR7 enzymatic inhibition. Both mechanisms converge on depletion of the cholesterol pool, consistent with the extensive transcriptional activation observed in enteroid monolayers upon 3 μM BAC cocktail exposure. A convergent signature of *HMGCR* upregulation, *ABCA1* downregulation, and sterolomically confirmed cholesterol disruption was independently observed in a BAC-exposed kidney-on-a-chip system (Brzoska et al., 2026), and transcriptional upregulation of biosynthesis genes following BAC exposure has been reported previously (Herron et al., 2019), together suggesting a conserved epithelial response across tissues.

The response extended beyond cholesterol. Enrichment of fatty acid metabolism pathways, including upregulation of *FASN*, *SCD*, and the elongases *ELOVL6* and *ELOVL7* (Figure 3.2.4; Supplementary Table 4), indicates concurrent activation of the SREBP1 lipogenic arm and points to broader membrane lipid remodeling. This is notable given the established role of lipid composition in maintaining epithelial barrier integrity and intestinal homeostasis, with disrupted lipid metabolism increasingly implicated in inflammatory bowel diseases including Crohn's disease and ulcerative colitis (Morelli et al., 2025; Pinelli et al., 2024).

The convergent enrichment of cell cycle and proliferative signaling pathways across both responding donors points to a pro-proliferative transcriptional response as a hallmark of acute BAC exposure. In HDO07, this response was characterized by upregulation of upstream proliferative activators including *MYC*, *CDK6*, *CDT1*, and *CDC25A*, alongside downregulation of CDK inhibitors *CDKN1A* and *CDKN2B* (Supplementary Table 3) (Dang, 2012; García-Gutiérrez et al., 2019). Additionally, enrichment of PI3K-Akt and canonical Wnt signaling pathways in this donor, alongside suppression of TGF-β target genes (Supplementary Figure 4), is consistent with a cellular environment being pushed toward growth and aligns with the known roles of these pathways in driving crypt progenitor expansion in the intestinal epithelium (Vanuytsel et al., 2013). These findings are notable given that PI3K-Akt activation has also been reported in proximal tubule epithelial cells following BAC exposure (Brzoska et al., 2026), suggesting this response is not unique to the intestinal epithelium. Furthermore, the activation of these pathways by a common dietary and personal care ingredient warrants attention, as dysregulated PI3K-Akt, canonical Wnt, and *MYC* signaling are among the most frequently implicated drivers of intestinal tumorigenesis (Dang, 2012; Vadlakonda et al., 2013; Vanuytsel et al., 2013).

In HDO11, the proliferative signal manifested further downstream, with broad induction of cyclins spanning the G1/S and G2/M phases (Figure 3.2.3), alongside upregulation of *MKI67*, encoding the proliferation marker Ki-67 (Figure 3.2.1B), pointing to a sweeping activation of cell cycle machinery at the transcriptional level. *MYC* sits downstream of both PI3K-Akt and canonical Wnt signaling (Supplementary Figure 4), as well as upstream of the cell cycle genes induced in HDO11 (Figure 3.2.3), positioning it as a potential mechanistic link (He et al., 1998; Vadlakonda et al., 2013). Viewed together, the two donors may represent the same *MYC*-centered program captured at different points: HDO07 at the level of upstream activation, with *MYC* induced and its repression targets *CDKN1A* and *CDKN2B* suppressed, and HDO11 at the level of downstream output, with broad induction of the cyclins and CDKs that *MYC* activates (Bretones et al., 2015).

The basis for this donor-specific variability in pathway activation remains unclear, but may reflect differences in baseline proliferative activity, receptor expression, or age. That the transcriptional response converges on a pro-proliferative program regardless of which specific genes are activated suggests BAC may engage multiple entry points into this pathway rather than a single toxicodynamic mechanism. This convergence was also evident at the level of individual genes. Although only 15 genes were differentially expressed in the same direction between HDO07 and HDO11 (Supplementary Table 2), several map onto the same proliferative axis. The MYC target *CDCA7* and the MYC cofactor *WDR5* were upregulated in both donors (Supplementary Table 2), providing two points of contact with the MYC program that dominated each donor's response (Osthus et al., 2005; Thomas et al., 2019). On the downregulated side, the growth-suppressive factors *IGFBP3* and *RASSF6* were reduced in both donors upon BAC exposure, consistent with loss of a pro-apoptotic Hippo-pathway brake (Supplementary Table 2,

Supplementary Figure 4D) (He et al., 2018). That this small gene set corroborates the MYC, PI3K-Akt, and cell cycle signals seen at the pathway level reinforces the conclusion that BAC engages a conserved pro-proliferative program across donors regardless of DEG magnitude. Whether this pro-proliferative program represents an adaptive compensatory response to BAC-induced growth inhibition or an early shift toward the dysregulated proliferative signaling implicated in intestinal tumorigenesis cannot be distinguished from these transcriptional data alone, particularly given the absence of functional proliferation measurements and the 16-hour exposure window.

Together, these proliferative and toxicokinetic gene changes point to a shared compensatory response to membrane stress upon 16-hour 3 μM BAC cocktail exposure. BAC-induced plasma membrane damage has been shown to trigger G0/G1 arrest in human epithelial cells via suppression of PI3K-Akt signaling and Cdc6 reduction (Kanno et al., 2023); the pro-proliferative transcriptional program observed here may therefore represent a compensatory response to this growth inhibition, with the epithelium simultaneously attempting to detoxify, restore lipid homeostasis, and resume division. Additionally, other reports have shown that at sub-toxic doses, higher chain BACs increase viability in Neuro2a cells (Herron et al., 2016), consistent with a pro-survival effect at concentrations below the cytotoxic threshold. Yet, whether this response translates to actual proliferation at the protein level warrants further investigation.

In contrast to the robust acute transcriptional response, chronic and repeated BAC exposure over 16 days produced minimal transcriptional disruption in HDO07, with only 10 DEGs detected at the 3 μM cocktail concentration and no significant DEGs at 50 nM or 500 nM

(Figure 3.3.1A). The predominant GO terms pointed to microvillus organization and brush border remodeling (Figure 3.3.1B), with upregulation of genes encoding established markers of differentiated enterocytes including *VIL1*, *KRT20*, and *CDHR5*, consistent with a differentiated, adapted epithelial state rather than one of ongoing stress. Paracellular permeability (Figure 3.3.2) and TEER (Supplementary Figure 5) were maintained across all concentrations throughout the exposure period, with LY diffusion declining modestly over time in a pattern consistent with continued monolayer maturation rather than BAC-specific barrier disruption (Figure 3.3.2D). These findings suggest that enteroid monolayers adapt to repeated luminal BAC exposure without sustained transcriptional disruption or barrier dysfunction, a marked contrast to the acute response, and underscore the capacity of the intestinal epithelium for functional resilience to commercially relevant BAC concentrations. Because maintenance conditions permit ongoing stem cell differentiation and limited proliferative turnover, it remains possible that continued exposure over longer timescales could shift this adapted state toward maladaptation. Multi-donor studies extending the chronic exposure window are warranted to test this possibility. Proteomic analyses are also needed to determine whether the acute transcriptional response and subsequent chronic adaptations are reflected at the protein level.

The acute transcriptional response to 3 μM BAC cocktail exposure varied substantially across donors, ranging from 1,349 DEGs in HDO11 to 355 in HDO07 to no detectable response in HDO03 (Figure 3.2.1; Figure 3.2.2). Rather than a limitation, this variability reflects a strength of the primary enteroid monolayer system, capturing inter-individual differences in intestinal biology that would be invisible in homogeneous transformed cell lines and underscoring the value of human primary models for toxicological risk assessment. This has direct relevance for population-level risk characterization, where a one-size-fits-all exposure threshold may

inadequately protect individuals whose intestinal biology renders them more susceptible to BAC toxicity.

The regulatory status of BACs remains unsettled and divergent across borders, which gives intestinal toxicity data added relevance. In the United States, the FDA has not finalized a GRAS/GRAE determination for BAC-containing antiseptics and continues to defer rulemaking pending additional safety data (FDA, 2019). The European Union (EU) has taken a more restrictive position: BACs are no longer approved for several consumer biocidal uses and the maximum residue level for BAC in food is set to not exceed 0.1 mg/kg (Merchel Piovesan Pereira & Tagkopoulos, 2019). Furthermore, the California EPA is actively evaluating QACs in consumer products under its Safer Consumer Products Program (California EPA, 2024). These parallel reassessments share a common limitation: they rely largely on ecological and animal toxicity data, with little direct evidence on the human small intestine. The findings presented here help address that gap and provide mechanistic context relevant to the ongoing evaluation of this widely used chemical class.

Strengths and Limitations

This study has several limitations worth acknowledging. The acute RNA-seq dataset from HDO07 represents a pilot experiment in a single donor, and while the addition of HDO11 and HDO03 strengthens the multi-donor characterization, the substantial inter-donor variability and absence of a response in HDO03 highlight the need for additional donors to support broader conclusions. The chronic experiment was conducted in a single donor at a single collection timepoint; inclusion of earlier timepoints in future studies would help determine when transcriptional adaptation occurs relative to the onset of exposure. The relaxed significance

threshold applied to the chronic dataset (FDR < 0.10) and the transcriptomics-only design are also worth noting, as whether the gene expression programs identified here translate to functional protein-level responses remains an open question that proteomics or functional proliferation assays could address.

Despite these limitations, the use of primary human duodenal enteroid monolayers from three independent donors represents a meaningful advance over transformed cell lines, capturing donor-specific transcriptional responses and inter-individual variability in a physiologically relevant human intestinal system. The Transwell format enabled simultaneous assessment of transcriptional and barrier endpoints under identical exposure conditions, and the inclusion of both acute and chronic exposure arms allowed direct comparison of short and long-term epithelial responses to luminal BAC.

Future directions

Expanding this model to additional donors across a broader range of ages and genetic backgrounds represents a natural next step toward characterizing population-level variability in intestinal BAC susceptibility. Whether the transcriptional programs identified here translate to functional responses remains an open question: protein quantification and sterolomics would establish whether the pro-proliferative and cholesterol biosynthesis signatures correspond to measurable changes at the protein and lipid level, respectively. Flow cytometry-based cell cycle analysis could further clarify whether treated monolayers show actual shifts in cell cycle state distribution. Finally, single-cell RNA-seq or computational deconvolution of bulk data would resolve whether these responses are uniform across epithelial cell types or concentrated in specific populations such as progenitors, secretory, or enterocyte lineages.

Conclusion

This study provides the first transcriptional characterization of the human intestinal response to BAC exposure using a primary human model system. Acute BAC exposure elicited a coordinated response involving xenobiotic detoxification, cholesterol biosynthesis, and pro-proliferative gene programs, which together point to epithelial adaptation to membrane stress. Chronic repeated exposure produced minimal transcriptional disruption and intact barrier function, suggesting the intestinal epithelium can adapt to sustained luminal BAC without cumulative injury. Given the continued rise in BAC use and human exposure, these findings underscore the importance of characterizing intestinal responses to this class of disinfectants at the site of first contact, and position primary enteroid monolayers as a valuable tool for doing so.

5. References

AOEC, Association of Occupational and Environmental Clinics, *AOEC Exposure Code Lookup*. (n.d.). Retrieved April 6, 2026, from http://www.aoecdata.org/ExpCodeLookup.aspx

Arian, C. M., Imaoka, T., Yang, J., Kelly, E. J., & Thummel, K. E. (2022). Gutsy science: *In vitro* systems of the human intestine to model oral drug disposition. *Pharmacology & Therapeutics*, *230*, 107962. https://doi.org/10.1016/j.pharmthera.2021.107962

Arian, C., O'Mahony, E., Bammler, T. K., Donowitz, M., Kelly, E. J., & Thummel, K. E. (2025). Human enteroid monolayers: A novel, functionally stable model for investigating oral drug disposition. *Drug Metabolism and Disposition*, *53*(1), 100002. https://doi.org/https://doi.org/10.1124/dmd.124.001551

Arnold, W. A., Blum, A., Branyan, J., Bruton, T. A., Carignan, C. C., Cortopassi, G., Datta, S., DeWitt, J., Doherty, A.-C., Halden, R. U., Harari, H., Hartmann, E. M., Hrubec, T. C., Iyer, S., Kwiatkowski, C. F., LaPier, J., Li, D., Li, L., Ortiz, J. G. M., … Xu, L. (2023).

Quaternary Ammonium Compounds: A Chemical Class of Emerging Concern. *Environmental Science & Technology*, *57*(20), 7645–7665. https://doi.org/10.1021/acs.est.2c08244

Barbara, G., Barbaro, M. R., Fuschi, D., Palombo, M., Falangone, F., Cremon, C., Marasco, G., & Stanghellini, V. (2021). Inflammatory and Microbiota-Related Regulation of the Intestinal Epithelial Barrier. *Frontiers in Nutrition*, *8*. https://doi.org/10.3389/fnut.2021.718356

Basit, A., Neradugomma, N. K., Wolford, C., Fan, P. W., Murray, B., Takahashi, R. H., Khojasteh, S. C., Smith, B. J., Heyward, S., Totah, R. A., Kelly, E. J., & Prasad, B. (2020). Characterization of Differential Tissue Abundance of Major Non-CYP Enzymes in Human. *Molecular Pharmaceutics*, *17*(11), 4114–4124. https://doi.org/10.1021/acs.molpharmaceut.0c00559

Betters, J. L., & Yu, L. (2010). NPC1L1 and cholesterol transport. *FEBS Letters*, *584*(13), 2740–2747. https://doi.org/10.1016/j.febslet.2010.03.030

Bonneau, L., Brossard, L., Noël, T., Perreaux, V., Bachir, L., Khan, A., Vales, S., & Mahe, M. M. (2025). Generation of Intestinal and Colonic Organoids Derived From Human Pluripotent Stem Cells. *Biology of the Cell*, *117*(12), e70044. https://doi.org/10.1111/boc.70044

Bretones, G., Delgado, M. D., & León, J. (2015). Myc and cell cycle control. *Biochimica et Biophysica Acta (BBA) - Gene Regulatory Mechanisms, Myc Proteins in Cell Biology and Pathology*, *1849*(5), 506–516. https://doi.org/10.1016/j.bbagrm.2014.03.013

Brunham, L. R., Kruit, J. K., Iqbal, J., Fievet, C., Timmins, J. M., Pape, T. D., Coburn, B. A., Bissada, N., Staels, B., Groen, A. K., Hussain, M. M., Parks, J. S., Kuipers, F., &

Hayden, M. R. (2006). Intestinal ABCA1 directly contributes to HDL biogenesis in vivo. *Journal of Clinical Investigation*, *116*(4), 1052–1062. https://doi.org/10.1172/JCI27352

Brzoska, M. N., Seguin, R. P., MacDonald, J. W., Yang, J., Lopez, V. A., Arnzen, S., Kelly, E. J., & Xu, L. (2026). Benzalkonium Chloride-Induced Nephrotoxicity in 2D Cultures and a Human Kidney-on-a-Chip System. *Environmental Science & Technology*. https://doi.org/10.1021/acs.est.5c15625

Campbell, J., Berry, J., & Liang, Y. (2019). Anatomy and Physiology of the Small Intestine. In *Shackelford's Surgery of the Alimentary Tract, 2 Volume Set* (pp. 817–841). Elsevier. https://doi.org/10.1016/B978-0-323-40232-3.00071-6

CDC. (2025, May 23). *National Exposure Report Home Page*. National Report on Human Exposure to Environmental Chemicals. https://www.cdc.gov/environmental-exposure-report/index.html

Clevers, H. (2013). The Intestinal Crypt, A Prototype Stem Cell Compartment. *Cell*, *154*(2), 274–284. https://doi.org/10.1016/j.cell.2013.07.004

Co, J. Y., Margalef-Català, M., Li, X., Mah, A. T., Kuo, C. J., Monack, D. M., & Amieva, M. R. (2019). Controlling Epithelial Polarity: A Human Enteroid Model for Host-Pathogen Interactions. *Cell Reports*, *26*(9), 2509-2520.e4. https://doi.org/10.1016/j.celrep.2019.01.108

Cortreau, M. M., Von Moltke, L. L., & Greenblatt, D. J. (2012). The Influence of Age and Sex on the Clearance of Cytochrome P450 3A Substrates. *Clinical Pharmacokinetics*, *44*, 33–60. https://doi.org/https://doi.org/10.2165/00003088-200544010-00002

Dang, C. V. (2012). MYC on the Path to Cancer. *Cell*, *149*(1), 22–35. https://doi.org/10.1016/j.cell.2012.03.003

Davis, H. R., Zhu, L., Hoos, L. M., Tetzloff, G., Maguire, M., Liu, J., Yao, X., Iyer, S. P. N., Lam, M.-H., Lund, E. G., Detmers, P. A., Graziano, M. P., & Altmann, S. W. (2004). Niemann-Pick C1 Like 1 (NPC1L1) Is the Intestinal Phytosterol and Cholesterol Transporter and a Key Modulator of Whole-body Cholesterol Homeostasis *. *Journal of Biological Chemistry*, *279*(32), 33586–33592. https://doi.org/10.1074/jbc.M405817200

EPA ChemExpo Knowledgebase. (n.d.). *C12-16-Alkylbenzyldimethylammonium Chlorides (DTXSID6028492)* [Dataset]. Retrieved April 6, 2026, from https://comptox.epa.gov/chemexpo/chemical/DTXSID6028492/

Feng, Y., Ren, T., Liu, S., Du, Z., Zhang, Y., Wang, P., Li, X., & Ma, J. (2025). The toxic effects of benzalkonium chloride on intestinal health in common carp (*Cyprinus carpio* L.): Potential role of intestinal microbiota-derived metabolites dysbiosis. *Environmental Chemistry and Ecotoxicology*, *7*, 2687–2699. https://doi.org/10.1016/j.enceco.2025.10.035

Flier, L. G. van der, & Clevers, H. (2009). Stem Cells, Self-Renewal, and Differentiation in the Intestinal Epithelium. *Annual Review of Physiology*, *71*(Volume 71, 2009), 241–260. https://doi.org/10.1146/annurev.physiol.010908.163145

García-Gutiérrez, L., Delgado, M. D., & León, J. (2019). MYC Oncogene Contributions to Release of Cell Cycle Brakes. *Genes*, *10*(3), 244. https://doi.org/10.3390/genes10030244

Gelberg, H. (2018). Pathophysiological Mechanisms of Gastrointestinal Toxicity. *Comprehensive Toxicology*, 139–178. https://doi.org/10.1016/B978-0-12-801238-3.10923-7

He, T.-C., Sparks, A. B., Rago, C., Hermeking, H., Zawel, L., da Costa, L. T., Morin, P. J., Vogelstein, B., & Kinzler, K. W. (1998). Identification of c-MYC as a Target of the APC Pathway. *Science*, *281*(5382), 1509–1512. https://doi.org/10.1126/science.281.5382.1509

He, Z., Zhao, T.-T., Jin, F., Li, J.-G., Xu, Y.-Y., Dong, H.-T., Liu, Q., Xing, P., Zhu, G.-L., Xu, H., & Miao, Z.-F. (2018). Downregulation of RASSF6 promotes breast cancer growth and chemoresistance through regulation of Hippo signaling. *Biochemical and Biophysical Research Communications*, *503*(4), 2340–2347. https://doi.org/10.1016/j.bbrc.2018.06.159

Herron, J. M., Hines, K. M., Tomita, H., Seguin, R. P., Cui, J. Y., & Xu, L. (2019). Multiomics Investigation Reveals Benzalkonium Chloride Disinfectants Alter Sterol and Lipid Homeostasis in the Mouse Neonatal Brain. *Toxicological Sciences*, *171*(1), 32–45. https://doi.org/https://doi.org/10.1093/toxsci/kfz139

Herron, J., Reese, R. C., Tallman, K. A., Narayanaswamy, R., Porter, N. A., & Xu, L. (2016). Identification of Environmental Quaternary Ammonium Compounds as Direct Inhibitors of Cholesterol Biosynthesis. *Toxicological Sciences*, *151*(2), 261–270. https://doi.org/10.1093/toxsci/kfw041

Hitosugi, M., Maruyama, K., & Takatsu, A. (1998). A case of fatal benzalkonium chloride poisoning. *International Journal of Legal Medicine*, *111*(5), 265–266. https://doi.org/10.1007/s004140050166

Horton, J. D., Goldstein, J. L., & Brown, M. S. (2002). SREBPs: Activators of the complete program of cholesterol and fatty acid synthesis in the liver. *The Journal of Clinical Investigation*, *109*(9), 1125–1131. https://doi.org/10.1172/JCI15593

Hrubec, T. C., Melin, V. E., Shea, C. S., Ferguson, E. E., Garofola, C., Repine, C. M., Chapman, T. W., Patel, H. R., Razvi, R. M., Sugrue, J. E., Potineni, H., Magnin-Bissel, G., & Hunt, P. A. (2017). Ambient and Dosed Exposure to Quaternary Ammonium Disinfectants Causes Neural Tube Defects in Rodents. *Birth Defects Research*, *109*(14), 1166–1178. https://doi.org/https://doi.org/10.1002/bdr2.1064

Hrubec, T. C., Seguin, R. P., Xu, L., Cortopassi, G., Datta, S., Hanlon, A., Lozano, A. J., McDonald, V. A., Healy, C. A., Anderson, T. C., Musse, N. A., & Williams, R. (2021). Altered toxicological endpoints in humans from common quaternary ammonium compounds disinfectant exposure. *Toxicology Reports*, *8*, 646–656. https://doi.org/https://doi.org/10.1016/j.toxrep.2021.03.006

Jeong, Y. E., Shea, K., & Ford, K. A. (2025). Unraveling Caco-2 cells through functional and transcriptomic assessments. *Regulatory Toxicology and Pharmacology*, *156*, 105771. https://doi.org/10.1016/j.yrtph.2025.105771

Kanno, S., Hirano, S., Monma-Otaki, J., Kato, H., Fukuta, M., Nakamura, Y., & Aoki, Y. (2023). Plasma membrane damage triggered by benzalkonium chloride and cetylpyridinium chloride induces G0/G1 cell cycle arrest via Cdc6 reduction in human lung epithelial cells. *The Journal of Toxicological Sciences*, *48*(2), 75–86. https://doi.org/10.2131/jts.48.75

Konstandi, M., & Johnson, E. O. (2023). Age-related modifications in CYP-dependent drug metabolism: Role of stress. *Frontiers in Endocrinology*, *14*. https://doi.org/10.3389/fendo.2023.1143835

Kraiczy, J., Ross, A. D. B., Forbester, J. L., Dougan, G., Vallier, L., & Zilbauer, M. (2019). Genome-Wide Epigenetic and Transcriptomic Characterization of Human-Induced

Pluripotent Stem Cell–Derived Intestinal Epithelial Organoids. *Cellular and Molecular Gastroenterology and Hepatology*, *7*(2), 285–288. https://doi.org/10.1016/j.jcmgh.2018.10.008

Lee, Y. Y., Erdogan, A., & Rao, S. S. C. (2014). How to Assess Regional and Whole Gut Transit Time With Wireless Motility Capsule. *Journal of Neurogastroenterology and Motility*, *20*(2), 265–270. https://doi.org/10.5056/jnm.2014.20.2.265

Li, D., Sangion, A., & Li, L. (2020). Evaluating consumer exposure to disinfecting chemicals against coronavirus disease 2019 (COVID-19) and associated health risks. *Environmental International*, *145*. https://doi.org/https://doi.org/10.1016/j.envint.2020.106108

Li, Z.-M., & Kannan, K. (2024). Quaternary Ammonium Compounds in Paired Human Urine and Feces: Relative Significance of Biliary Elimination. *Environmental Science & Technology Letters*, *11*(6), 533–538. https://doi.org/10.1021/acs.estlett.4c00372

Lopez, V. A., Lim, J. J., Seguin, R. P., Dempsey, J. L., Kuzman, G., Cui, J. Y., & Xu, L. (2024). Oral exposure to benzalkonium chlorides in male and female mice reveals alteration of the gut microbiome and bile acid profile. *Toxicological Sciences*, *202*(2), 265–277. https://doi.org/https://doi.org/10.1093/toxsci/kfae116

Melin, V. E., Potineni, H., Hunt, P., Griswold, J., Siems, B., Werre, S. R., & Hrubec, T. C. (2014). Exposure to common quaternary ammonium disinfectant decreases fertility in mice. *Reproductive Toxicology*, *50*, 163–170. https://doi.org/https://doi.org/10.1016/j.reprotox.2014.07.071

Merchel Piovesan Pereira, B., & Tagkopoulos, I. (2019). Benzalkonium Chlorides: Uses, Regulatory Status, and Microbial Resistance. *Applied and Environmental Microbiology*, *85*(13). https://doi.org/doi:%20https://doi.org/10.1128/aem.00377-19

Morelli, M., Savova, M. V., Queiroz, K., Harms, A. C., & Hankemeier, T. (2025). Cytokine-Induced Barrier Dysfunction and Lipid Signaling in a Gut-On-Chip Model. *The FASEB Journal*, *39*(19), e71059. https://doi.org/10.1096/fj.202501685R

Oda, S., Kato, Y., Hatakeyama, M., Iwamura, A., Fukami, T., Kume, T., Yokoi, T., & Nakajima, M. (2017). Evaluation of Expression and Glycosylation Status of UGT1A10 in Supersomes and Intestinal Epithelial Cells with a Novel Specific UGT1A10 Monoclonal Antibody. *Drug Metabolism and Disposition*, *45*(9), 1027–1034. https://doi.org/10.1124/dmd.117.075291

O'Mahony, E. T., Arian, C. M., Aryeh, K. S., Wang, K., Thummel, K. E., & Kelly, E. J. (2025). Human intestinal enteroids: Nonclinical applications for predicting oral drug disposition, toxicity, and efficacy. *Pharmacology & Therapeutics*, *273*, 108879. https://doi.org/10.1016/j.pharmthera.2025.108879

Osthus, R. C., Karim, B., Prescott, J. E., Smith, B. D., McDevitt, M., Huso, D. L., & Dang, C. V. (2005). The Myc Target Gene JPO1/CDCA7 Is Frequently Overexpressed in Human Tumors and Has Limited Transforming Activity In vivo. *Cancer Research*, *65*(13), 5620–5627. https://doi.org/10.1158/0008-5472.CAN-05-0536

Pinelli, M., Makdissi, S., Scur, M., Parsons, B. D., Baker, K., Otley, A., MacIntyre, B., Nguyen, H. D., Kim, P. K., Stadnyk, A. W., & Di Cara, F. (2024). Peroxisomal cholesterol metabolism regulates yap-signaling, which maintains intestinal epithelial barrier function and is altered in Crohn's disease. *Cell Death & Disease*, *15*(7), 536. https://doi.org/10.1038/s41419-024-06925-x

Rao, S. S. C., Kuo, B., McCallum, R. W., Chey, W. D., DiBaise, J. K., Hasler, W. L., Koch, K. L., Lackner, J. M., Miller, C., Saad, R., Semler, J. R., Sitrin, M. D., Wilding, G. E., &

Parkman, H. P. (2009). Investigation of Colonic and Whole-Gut Transit With Wireless Motility Capsule and Radiopaque Markers in Constipation. *Clinical Gastroenterology and Hepatology*, *7*(5), 537–544. https://doi.org/10.1016/j.cgh.2009.01.017

Rasmi, R. R., Kovatich, R., Farley, A., Sakthivel, K. M., Takiar, V., & Sertorio, M. (2025). Targeting SREBP2 in cancer progression: Molecular mechanisms, oncogenic crosstalk, and therapeutic interventions. *Cellular Signalling*, *135*, 112044. https://doi.org/10.1016/j.cellsig.2025.112044

Rong, S., Cortés, V. A., Rashid, S., Anderson, N. N., McDonald, J. G., Liang, G., Moon, Y.-A., Hammer, R. E., & Horton, J. D. (2017). Expression of SREBP-1c Requires SREBP-2-mediated Generation of a Sterol Ligand for LXR in Livers of Mice. *eLife*, *6*, e25015. https://doi.org/10.7554/eLife.25015

Sanidad, K. Z., Yang, H., Wang, W., Ozay, E. I., Yang, J., Gu, M., Karner, E., Zhang, J., Kim, D., Minter, L. M., Xiao, H., & Zhang, G. (2018). Effects of Consumer Antimicrobials Benzalkonium Chloride, Benzethonium Chloride, and Chloroxylenol on Colonic Inflammation and Colitis-Associated Colon Tumorigenesis in Mice. *Toxicological Sciences*, *163*(2), 490–499. https://doi.org/10.1093/toxsci/kfy045

Sansom, O. J., Meniel, V. S., Muncan, V., Phesse, T. J., Wilkins, J. A., Reed, K. R., Vass, J. K., Athineos, D., Clevers, H., & Clarke, A. R. (2007). Myc deletion rescues Apc deficiency in the small intestine. *Nature*, *446*(7136), 676–679. https://doi.org/10.1038/nature05674

Sato, T., Stange, D. E., Ferrante, M., Vries, R. G. J., Es, J. H. van, Brink, S. van den, Houdt, W. J. van, Pronk, A., Gorp, J. van, Siersema, P. D., & Clevers, H. (2011). Long-term Expansion of Epithelial Organoids From Human Colon, Adenoma, Adenocarcinoma, and

Barrett's Epithelium. *Gastroenterology*, *141*(5), 1762–1772. https://doi.org/10.1053/j.gastro.2011.07.050

Sato, T., Vries, R. G., Snippert, H. J., van de Wetering, M., Barker, N., Stange, D. E., van Es, J. H., Abo, A., Kujala, P., Peters, P. J., & Clevers, H. (2009). Single Lgr5 stem cells build crypt-villus structures in vitro without a mesenchymal niche. *Nature*, *459*(7244), 262–265. https://doi.org/10.1038/nature07935

Seguin, R. P., Herron, J. M., Lopez, V., Dempsey, J. L., & Xu, L. (2019). Metabolism of Benzalkonium Chlorides by Human Hepatic Cytochromes P450. *Chemical Research in Toxicology*, *32*(12), 2466–2478. https://doi.org/https://doi.org/10.1021/acs.chemrestox.9b00293

Sun, H., Chow, E. C., Liu, S., Du, Y., & Pang, K. S. (2008). The Caco-2 cell monolayer: Usefulness and limitations. *Expert Opinion on Drug Metabolism & Toxicology*, *4*(4), 395–411. https://doi.org/10.1517/17425255.4.4.395

Thomas, L. R., Adams, C. M., Wang, J., Weissmiller, A. M., Creighton, J., Lorey, S. L., Liu, Q., Fesik, S. W., Eischen, C. M., & Tansey, W. P. (2019). Interaction of the oncoprotein transcription factor MYC with its chromatin cofactor WDR5 is essential for tumor maintenance. *Proceedings of the National Academy of Sciences*, *116*(50), 25260–25268. https://doi.org/10.1073/pnas.1910391116

United States Food and Drug Administration, Department of Health and Human Services. (2019, April 12). *Safety and Effectiveness of Consumer Antiseptic Rubs; Topical Antimicrobial Drug Products for Over-the-Counter Human Use*. https://www.federalregister.gov/documents/2019/04/12/2019-06791/safety-and-effectiveness-of-consumer-antiseptic-rubs-topical-antimicrobial-drug-products-for

Vadlakonda, L., Pasupuleti, M., & Pallu, R. (2013). Role of PI3K-AKT-mTOR and Wnt Signaling Pathways in Transition of G1-S Phase of Cell Cycle in Cancer Cells. *Frontiers in Oncology*, *3*, 85. https://doi.org/10.3389/fonc.2013.00085

Vanuytsel, T., Senger, S., Fasano, A., & Shea-Donohue, T. (2013). Major signaling pathways in intestinal stem cells. *Biochimica et Biophysica Acta (BBA) - General Subjects, Biochemistry of Stem Cells*, *1830*(2), 2410–2426. https://doi.org/10.1016/j.bbagen.2012.08.006

Vieira, L. S., Seguin, R., Xu, L., & Wang, J. (2024). Interaction and Transport of Benzalkonium Chlorides by the Organic Cation and Multidrug and Toxin Extrusion Transporters. *Drug Metabolism and Disposition*, *52*(4), 312–321. https://doi.org/doi:https://doi.org/10.1124/dmd.123.001625

Wang, K., Tsang, Y. P., Thummel, K. E., Kelly, E. J., Mao, Q., & Unadkat, J. D. (2026). Effect of proinflammatory cytokines on intestinal drug transporters in human enteroid monolayers. *Drug Metabolism and Disposition*, *54*(1), 100208. https://doi.org/10.1016/j.dmd.2025.100208

Wentworth, A. B., Yiannias, J. A., Davis, M. D. P., & Killian, J. M. (2016). Benzalkonium Chloride: A Known Irritant and Novel Allergen. *Dermatitis®*, *27*(1), 14–20. https://doi.org/10.1097/DER.0000000000000160

Wilson, J. T., & Burr, I. M. (1975). Benzalkonium chloride poisoning in infant twins. *American Journal of Diseases of Children*, *129*(10), 1208–1209. https://doi.org/10.1001/archpedi.1975.02120470054015

Xie, F., Ding, X., & Zhang, Q.-Y. (2016). An update on the role of intestinal cytochrome P450 enzymes in drug disposition. *Acta Pharmaceutica Sinica. B*, *6*(5), 374–383. https://doi.org/10.1016/j.apsb.2016.07.012

Yan, R., Cao, P., Song, W., Li, Y., Wang, T., Qian, H., Yan, C., & Yan, N. (2021). Structural basis for sterol sensing by Scap and Insig. *Cell Reports*, *35*(13), 109299. https://doi.org/10.1016/j.celrep.2021.109299

Zheng, G., Webster, T., & Salamova, A. (2021). Quaternary Ammonium Compounds: Bioaccumulation Potentials in Humans and Levels in Blood before and during the COVID-19 Pandemic. *Environmental Science & Technology*, *55*(21), 14689–14698. https://doi.org/https://doi.org/10.1021/acs.est.1c01654

6. Supplementary Material

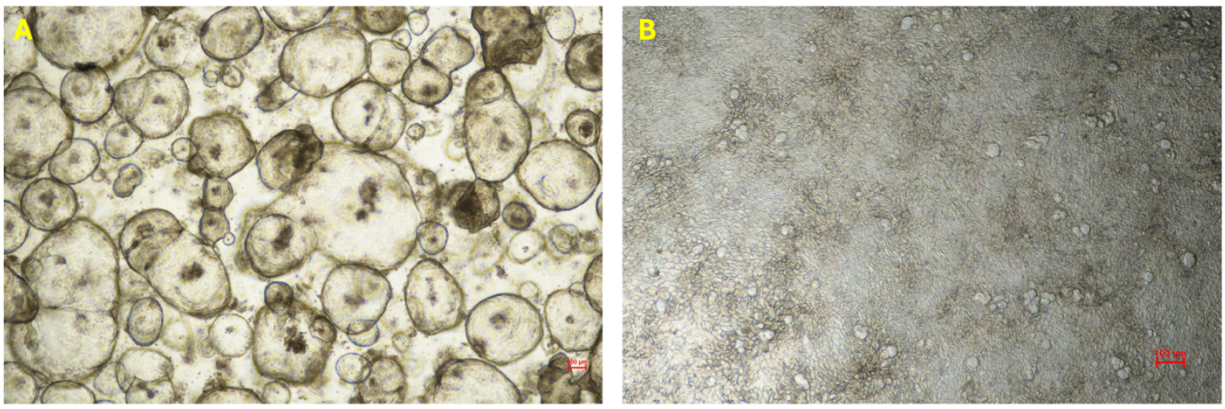

Supplementary Figure 1. Brightfield images of undifferentiated organoids and differentiated enteroid monolayers. [A] Undifferentiated human intestinal organoids grown in Matrigel domes. **[B]** Differentiated enteroid monolayer on a 24-well Transwell insert following 14 days of culture. Both images acquired at 4x magnification on a Nikon Eclipse Ti microscope. Scale bars = 100 µm.

Supplementary Table 1. Primary and Secondary Antibodies for Immunocytochemistry

Target	Host Species	Vendor	Catalog No.	Dilution
ZO-3	Rabbit	Abcam	ab181991	1:100
Occludin	Mouse	Abcam	ab242202	1:100

MRP3	Rabbit	Abcam	ab204322	1:100
Ki-67	Rabbit	Abcam	ab92742	1:100
Goat anti-rabbit IgG, Alexa Fluor 594	Goat	Invitrogen	A-11037	1:1000
Goat anti-rabbit IgG, Alexa Fluor 488	Goat	Invitrogen	A-11008	1:1000
Goat anti-mouse IgG, Alexa Fluor 488	Goat	Invitrogen	A-21141	1:1000
Hoechst 33342	N/A	Invitrogen	H3570	0.5 µg/mL

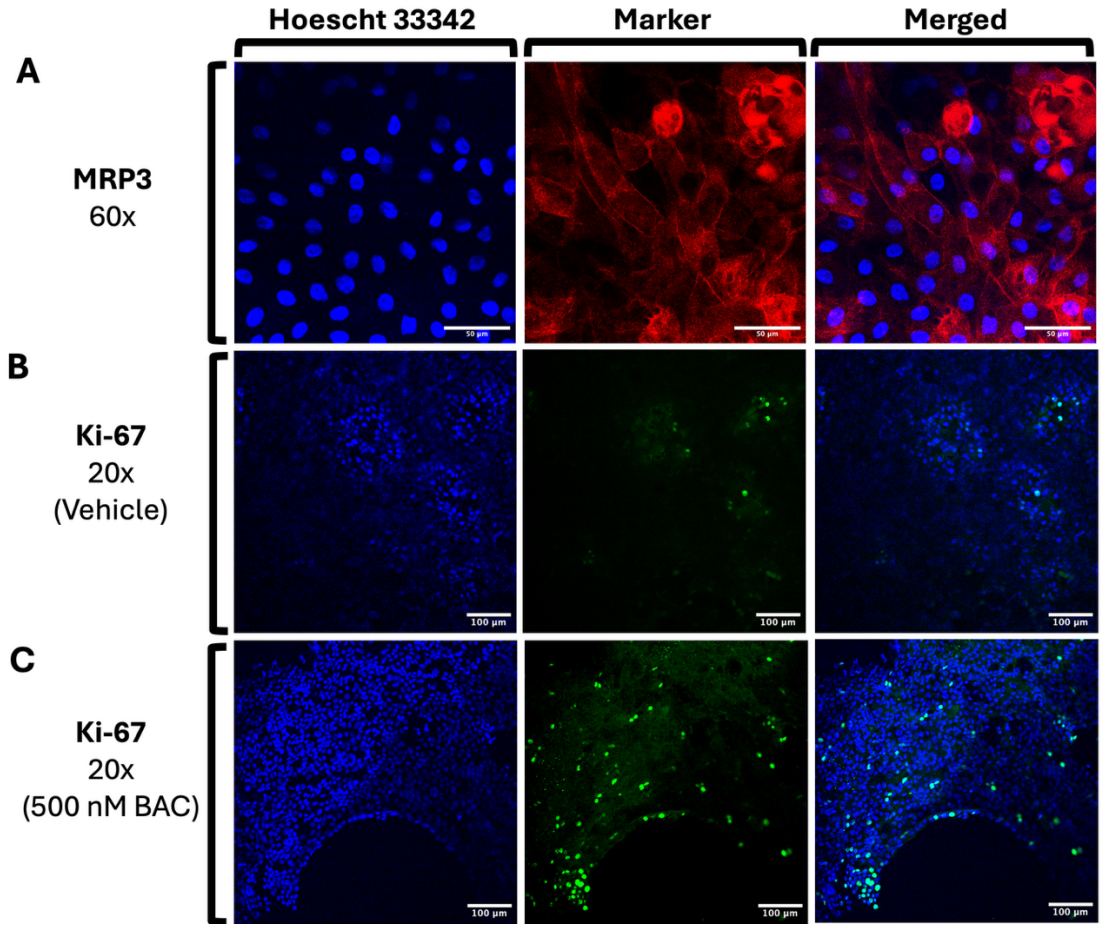

Supplementary Figure 2. Immunocytochemical staining of MRP3 and Ki-67 in human enteroid monolayers derived from a single donor. [A] MRP3 staining (red) at 60x magnification demonstrates expression of this efflux transporter. **[B, C]** Ki-67 staining (green) at 20x magnification in vehicle-treated **[B]** and 500 nM BAC-treated **[C]** monolayers. Nuclei are counterstained with Hoechst 33342 (blue). Scale bars: 50 µm **[A];** 100 µm **[B, C].**

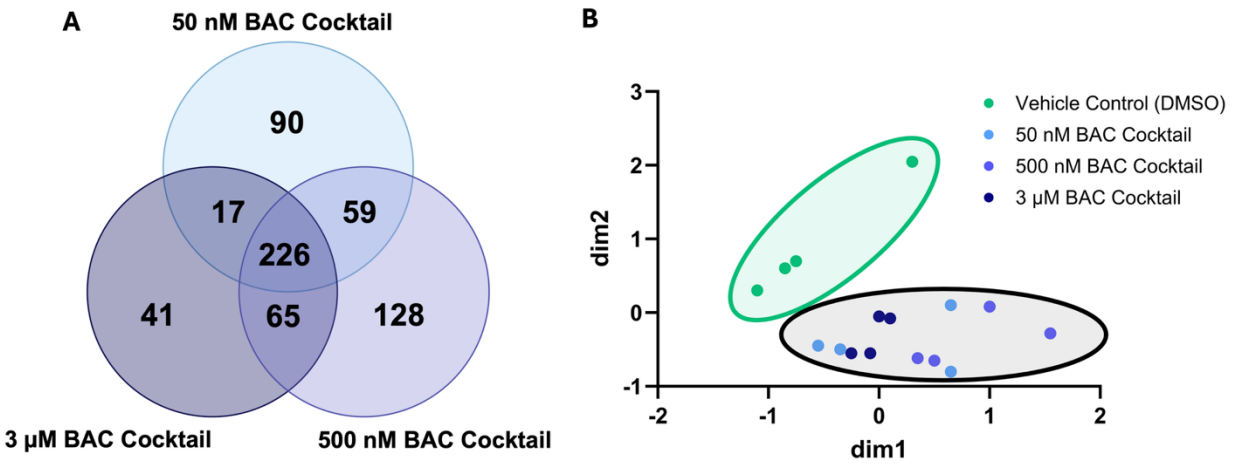

Supplementary Figure 3. Clustering of 16-hour BAC cocktail DEGs and MDS plot of HDO07 RNA-seq samples. [A] Venn diagram depicting the number of differentially expressed genes (DEGs; FDR < 0.05) unique to and shared across 50 nM, 500 nM, and 3 µM BAC cocktail conditions relative to vehicle control in HDO07. **[B]** Multidimensional scaling (MDS) plot of HDO07 samples colored by treatment condition. Each point represents one technical replicate (n=4 per condition). Ellipses denote approximate grouping of vehicle control and BAC-treated samples.

Supplementary Table 2. Differentially expressed genes concordant in direction between HDO07 and HDO11 following 16-hour 3 µM BAC cocktail exposure.

	HDO07		HDO11	
Gene	**log_2FC**	**adj. p-value**	**log_2FC**	**adj. p-value**
CDCA7	0.824	1.21E-02	*1.028*	2.71E-05
DBF4	0.867	9.00E-04	*0.737*	3.92E-02
TMEM150C	0.728	6.00E-04	*0.714*	2.95E-02
PAIP2B	0.796	4.77E-02	*0.523*	3.20E-02
TIFA	0.688	1.31E-02	*0.428*	3.83E-02
SLC12A2	0.483	3.70E-02	*0.355*	1.63E-02
KCNE3	0.635	1.10E-03	*0.34*	1.13E-02
WDR5	0.509	1.13E-02	*0.263*	2.42E-02
MEF2D	-0.508	3.69E-02	*-0.206*	2.64E-02
RASSF6	-0.606	6.00E-04	*-0.209*	1.88E-02
TSC22D2	-0.587	7.90E-03	*-0.272*	3.52E-02
IKZF2	-0.94	5.00E-04	*-0.274*	4.78E-02
IGFBP3	-0.877	1.00E-04	*-0.277*	2.64E-02
MUC3A	-0.743	2.59E-02	*-0.465*	6.50E-03
RAB3B	-0.6	2.55E-02	*-0.516*	1.40E-03

Supplementary Table 3. Differentially expressed genes associated with cell cycle and signaling pathways in HDO07 following acute 16-hour exposure to 3 µM BAC cocktail relative to vehicle control.

Gene	log_2FC	adj. p-value
Cell Cycle		
MYC	2.067	3.74E-10
DBF4	0.867	9.24E-04
CDK6	0.986	6.97E-08
CDKN2B	-1.136	4.84E-05
CCND3	-0.557	4.18E-04
CDKN1A	-0.543	2.42E-03
GADD45A	-0.535	3.86E-02
PI3K-Akt Signaling		
MYC	2.067	3.74E-10
FGF20	1.546	4.39E-03
MYB	1.188	1.17E-05
IRS1	0.967	1.55E-07
CDK6	0.986	6.97E-08
PIK3R1	0.722	1.78E-07
KITLG	0.609	8.26E-04
FGFR2	0.586	1.13E-03
ITGA6	0.405	4.46E-02
CREB3L3	-1.709	2.21E-05
PIK3R3	-0.943	1.54E-04
SGK2	-0.741	1.30E-02
TGFA	-0.499	1.70E-03
CDKN1A	-0.543	2.42E-03
CCND3	-0.557	4.18E-04
Canonical Wnt Signaling		
AXIN2	*2.79*	1.32E-08
MYC	*2.067*	3.74E-10
NKD1	*1.586*	6.42E-05
LGR5	*1.437*	3.07E-03
RNF43	*1.182*	2.21E-09
ZNRF3	*1.112*	8.20E-06
BAMBI	*1.073*	1.61E-02
CDKN2B	*-1.136*	4.84E-05
CCND3	*-0.557*	4.18E-04
FZD5	*-0.471*	9.49E-03
TGF-β Signaling		
MYC	2.067	3.74E-10
RGMB	1.739	7.88E-09
TGIF1	1.537	2.35E-09
BMP4	1.1	2.45E-08
BAMBI	1.073	1.61E-02
TGFBR2	0.567	3.92E-04

BMP7	0.527	4.82E-03
BMP2	-0.766	1.65E-05
CDKN2B	-1.136	4.84E-05

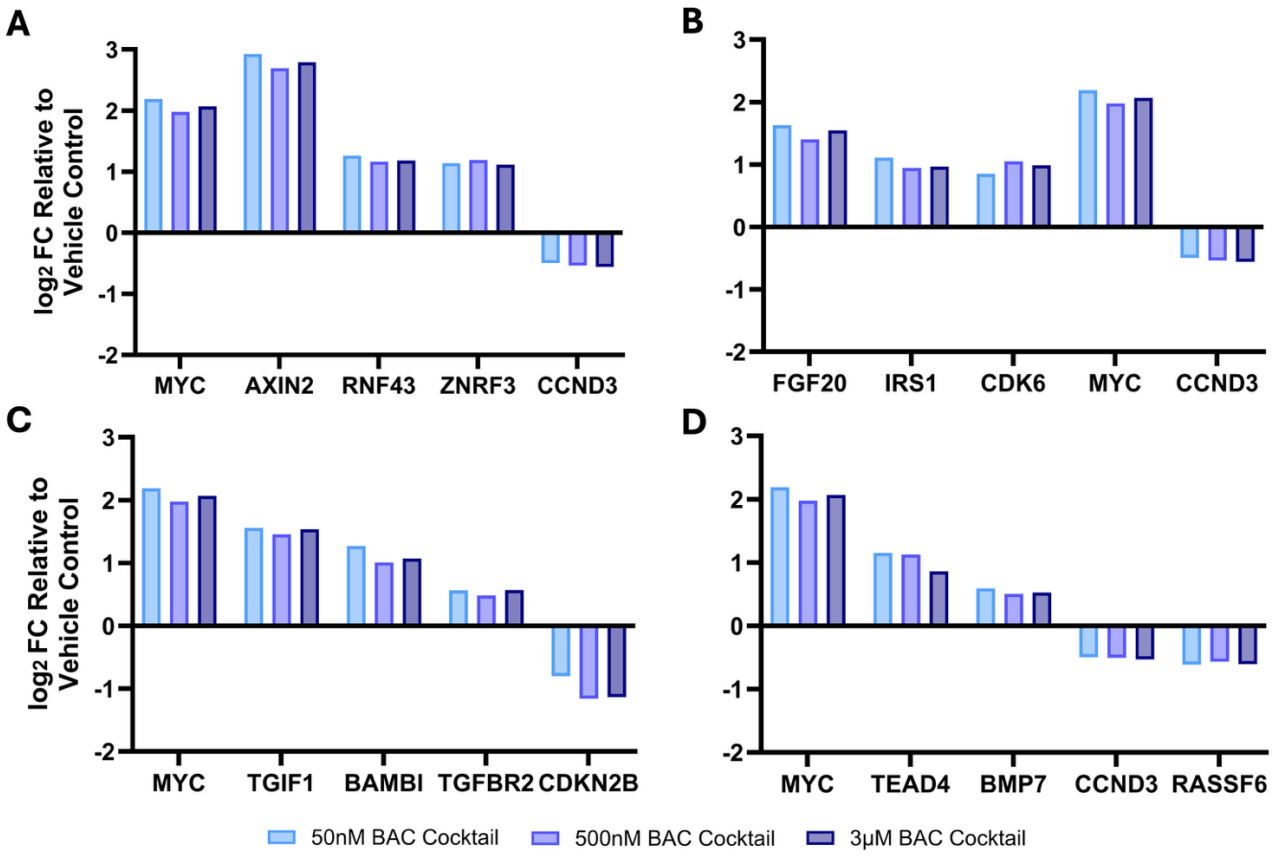

Supplementary Figure 4. Differentially expressed genes in PI3K-Akt, Canonical Wnt, TGF-β, and Hippo signaling pathways in HDO07 following 16-hour BAC cocktail exposure. Log_2 fold change relative to vehicle control is shown for selected DEGs ($p < 0.05$) in **[A]** PI3K-Akt signaling, **[B]** Canonical Wnt signaling, **[C]** TGF-β signaling, and **[D]** Hippo signaling. Bars represent 50 nM (light blue), 500 nM (medium blue), and 3 µM (dark navy) BAC cocktail.

Supplementary Table 4. Differentially expressed genes involved in lipid homeostasis in HDO11 following 16-hour 3 µM BAC cocktail exposure.

Gene	log_2FC	p-value
Cholesterol Signaling & Feedback		
INSIG1	0.459	6.58E-05
INSIG2	0.347	2.00E-03
PCSK9	0.545	1.97E-04
LDLR	0.296	2.00E-03
ABCA1	-0.337	1.80E-02

Cholesterol Synthesis		
ACAT1	0.547	5.00E-03
ACAT2	0.654	8.90E-06
HMGCS1	0.632	1.21E-05
HMGCR	0.434	1.85E-04
MVK	0.509	6.19E-04
MVD	0.679	7.91E-06
FDPS	0.501	2.84E-05
IDI1	0.479	3.80E-04
FDFT1	0.457	2.01E-04
SQLE	0.350	5.00E-03
LSS	0.576	8.56E-06
CYP51A1	0.212	2.80E-02
MSMO1	0.318	8.00E-03
NSDHK	0.290	4.90E-02
HSD17B7	0.704	4.64E-05
EBP	0.353	4.00E-03
LBR	0.214	2.10E-02
DHCR7	0.297	2.00E-03
DHCR24	0.187	2.90E-02
Lipid Metabolism		
ACSL1	0.269	1.00E-03
ACOX2	0.688	1.90E-02
HADH	0.602	3.62E-04
HMGCS2	0.403	3.70E-02
FASN	0.335	1.10E-02
SCD	0.287	1.10E-02
ELOVL6	0.278	2.10E-02
ELOVL7	0.236	4.50E-02
LPCAT1	0.279	2.00E-03
PLA2G7	1.585	3.00E-02
PLA2G2A	0.834	4.40E-02
FILIP1L	0.272	1.60E-02
LIPA	0.516	3.04E-04
LIPG	0.379	1.00E-03

Supplementary Table 5. Differentially expressed genes involved in xenobiotic metabolism and disposition following 16-hour 3 µM BAC cocktail exposure. *Denotes shared differential expression between donors.

Class	Gene	log_2FC	adj. p-value	Donor
Phase I Enzymes				
Carboxylesterase (CES)	*CES1*	0.703	2.10E-02	HDO11

Epoxide hydrolase (EPHX)	*EPHX2*	-0.517	2.10E-02	HDO11
Aldo-keto reductase (AKR)	*AKR1B1*	0.465	3.80E-02	HDO11
Aldo-keto reductase (AKR)	*AKR1C3*	0.307	2.30E-02	HDO11
Aldo-keto reductase (AKR)	*AKR7A2*	0.207	2.20E-02	HDO11
Aldo-keto reductase (AKR)	*AKR1C4*	1.116	1.20E-02	HDO11
Aldehyde dehydrogenase (ALDH)	*ALDH7A1*	0.697	1.78E-05	HDO11
Aldehyde dehydrogenase (ALDH)	*ALDH9A1*	0.281	3.00E-03	HDO11
Aldehyde dehydrogenase (ALDH)	*ALDH2*	0.274	2.58E-04	HDO11
Aldehyde dehydrogenase (ALDH)	*ALDH18A1*	0.253	1.00E-03	HDO11
Aldehyde dehydrogenase (ALDH)	*ALDH3B1*	-0.64	2.00E-03	HDO07
Cytochrome P450 (CYP)	*CYP4F12*	0.517	3.10E-02	HDO11
Cytochrome P450 (CYP)	*CYP2S1*	-0.311	1.60E-02	HDO11
Cytochrome P450 (CYP)	*CYP51A1*	0.212	2.80E-02	HDO11
Cytochrome P450 (CYP)	*CYP3A5*	-0.208	1.60E-02	HDO11
Superoxide dismutase (SOD)	*SOD2*	0.201	2.50E-02	HDO11
Phase II Enzymes				
Glutathione S-transferase (GST)	*GSTA2*	1.442	8.00E-03	HDO11
Glutathione S-transferase (GST)	*GSTA1*	0.627	4.00E-03	HDO11
Sulfotransferase (SULT)	*SULT1A3*	4.678	3.00E-02	HDO11
Sulfotransferase (SULT)	*SLX1A-SULT1A3*	0.467	4.50E-02	HDO11
UDP-glucuronosyltransferase (UGT)	*UGT1A10*	0.271	3.00E-03	HDO11
UDP-glucuronosyltransferase (UGT)	*UGT1A1*	0.247	1.50E-02	HDO11
Uptake Transporters				
Solute Carrier (SLC; ASCT1)	*SLC1A4*	1.068	1.70E-02	HDO11
Solute Carrier (SLC; GLUT3)	*SLC2A3*	-0.91	1.80E-02	HDO11
Solute Carrier (SLC; LAT2)	*SLC7A8*	0.47	3.00E-03	HDO11
Solute Carrier (SLC; TaurT)	*SLC6A6*	0.613	9.47E-03	HDO07
Solute Carrier (SLC; PAT1)	*SLC36A1*	0.442	1.40E-02	HDO11
Solute Carrier (SLC; ATB0)	*SLC6A14*	0.315	1.30E-02	HDO11
Solute Carrier (SLC; CAT2)	*SLC7A2*	0.9278	3.81E-02	HDO07
Solute Carrier (SLC; ASCT2)	*SLC1A5*	-0.238	3.00E-02	HDO11
Solute Carrier (SLC; FATP3)	*SLC27A3*	0.611	1.60E-02	HDO11
Solute Carrier (SLC; SGLT4)	*SLC5A9*	-0.42	4.50E-02	HDO11
Solute Carrier (SLC; G6PT)	*SLC37A4*	0.367	1.90E-02	HDO11
Solute Carrier (SLC; SERT)	*SLC6A4*	1.792	2.00E-02	HDO11
Solute Carrier (SLC; ThTr2)	*SLC19A3*	1.046	3.20E-04	HDO07
Solute Carrier (SLC; OATv1)	*SLC17A4*	-0.7953	2.31E-03	HDO07
*Solute Carrier (SLC; NKCC1)	*SLC12A2*	0.355, 0.483	1.6E-02, 3.7E-02	HDO11, HDO07
Solute Carrier (SLC; DIC)	*SLC25A10*	-0.308	1.90E-02	HDO11
Solute Carrier (SLC; MTPPT)	*SLC25A19*	0.9111	1.77E-02	HDO07
Solute Carrier (SLC; ANT2)	*SLC25A5*	-0.283	6.97E-04	HDO11

Solute Carrier (SLC; ANT3)	*SLC25A6*	-0.197	3.70E-02	HDO11
Solute Carrier (SLC; MCT2)	*SLC16A7*	0.657	3.40E-02	HDO11
Solute Carrier (SLC; MCT8)	*SLC16A2*	0.353	4.10E-02	HDO11
Solute Carrier (SLC; CNT3)	*SLC28A3*	-0.578	6.65E-04	HDO11
Solute Carrier (SLC)	*SLC35G1*	0.514	2.55E-04	HDO11
Solute Carrier (SLC; AT2)	*SLC33A2*	0.343	3.50E-02	HDO11
Solute Carrier (SLC; UGTrel7)	*SLC35D1*	0.285	3.00E-02	HDO11
Solute Carrier (SLC)	*SLC22A23*	-0.5478	3.79E-02	HDO07
Solute Carrier (SLC)	*SLC37A1*	-0.4296	4.78E-02	HDO07
Solute Carrier (SLC; RFT1)	*SLC52A1*	-1.11	1.33E-02	HDO07
Solute Carrier (SLC; POMT)	*SLC45A3*	0.263	1.60E-02	HDO11
Solute Carrier (SLC; ZIP8)	*SLC39A8*	0.505	2.30E-02	HDO11
Solute Carrier (SLC; ZIP5)	*SLC39A5*	0.456	1.20E-02	HDO11
Solute Carrier (SLC; ZIP10)	*SLC39A10*	0.6354	1.21E-02	HDO07
Solute Carrier (SLC; ZIP11)	*SLC39A11*	0.209	2.50E-02	HDO11
Efflux Transporters				
ATP-Binding Cassette (ABC)	*ABCA1*	-0.337	1.80E-02	HDO11
ATP-Binding Cassette (ABC)	*ABCB6*	0.314	4.50E-02	HDO11
ATP-Binding Cassette (ABC; MRP5)	*ABCC5*	-0.266	4.20E-02	HDO11
Solute Carrier (SLC; ZnT10)	*SLC30A10*	1.413	3.80E-02	HDO11

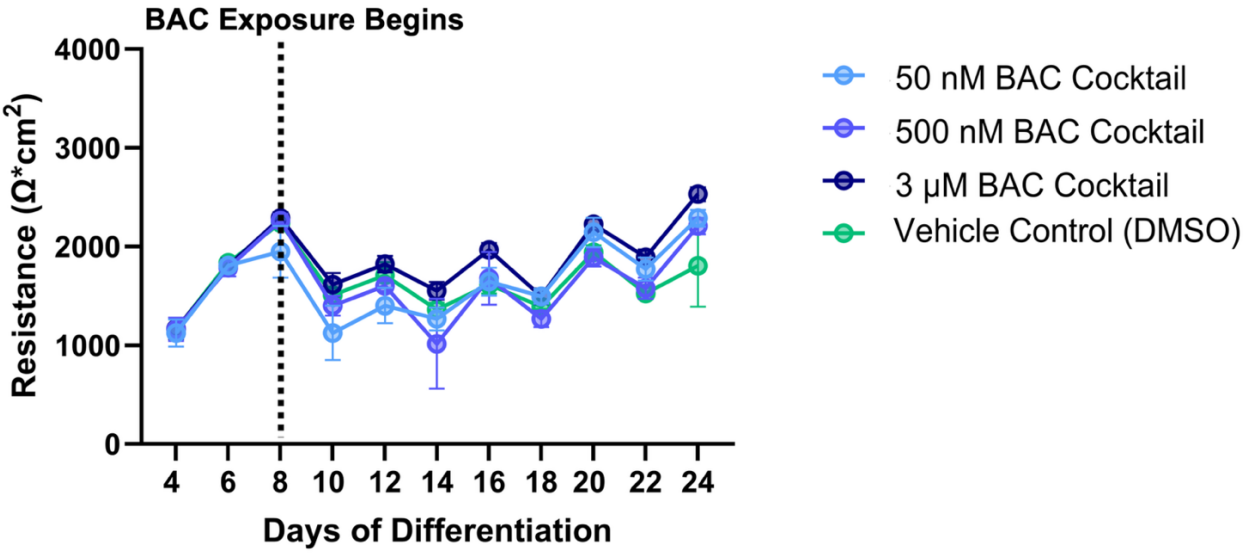

Supplementary Figure 5. Transepithelial electrical resistance is maintained throughout chronic BAC exposure. Adjusted TEER (Ω•cm^2) measured prior to media changes: every two days from Day 4 through Day 24 or differentiation. Dashed vertical line indicates onset of apical BAC cocktail exposure at Day 8 of differentiation. All conditions maintained a mean resistance above 1000 Ω•cm^2 throughout the exposure period, with no sustained change observed in BAC-treated monolayers relative to vehicle controls. BAC cocktail composed of C_{12}-, C_{14}-, and C_{16}-

BAC at a 40:50:10 molar ratio. Data represents mean ± SD; n = 4 technical replicates per condition from a single donor experiment (HDO07; 1 biological replicate).